Title

Densely populated biofilms and linked iron and sulfur cycles in the fractured-rock continental subsurface

Authors

Schuler, Christopher J
Patsis, Amanda
Alexander, Scott C
et al.

Publication Date

2024-06-01

DOI

10.1016/j.gca.2024.04.019

Geochimica et Cosmochimica Acta 375 (2024) 229–246

Contents lists available at ScienceDirect

Geochimica et Cosmochimica Acta

journal homepage: www.elsevier.com/locate/gca

Densely populated biofilms and linked iron and sulfur cycles in the fractured-rock continental subsurface

Christopher J. Schuler [a,b], Amanda Patsis [a,b], Scott C. Alexander [a,1], David Hsu [b,c], William S. Dowd [d], Woonghee Lee [a], Sarick L. Matzen [e], Matthew A. Marcus [f], Cody S. Sheik [g,h], Jill M. McDermott [d], Peter K. Kang [a], Cara M. Santelli [a,b], Brandy M. Toner [a,e,*]

[a] University of Minnesota – Twin Cities, Department of Earth and Environmental Sciences, 116 Church St SE, Minneapolis, MN 55455, United States
[b] University of Minnesota – Twin Cities, Biotechnology Institute, 1479 Gortner Avenue St. Paul, MN 55108, United States
[c] University of Minnesota – Twin Cities, Department of Plant and Microbial Biology, 1479 Gortner Avenue St. Paul, MN 55108, United States
[d] Lehigh University, Department of Earth and Environmental Science, W Packer Ave, Bethlehem, PA 18015, United States
[e] University of Minnesota – Twin Cities, Department of Soil, Water, and Climate, 1991 Upper Buford Cir, St. Paul, MN 55108, United States
[f] Lawrence Berkeley National Laboratory, Advanced Light Source, 6 Cyclotron Rd, Berkeley, CA 94720, United States
[g] University of Minnesota – Duluth, Large Lakes Observatory, 2205 E 5th St, Duluth, MN 55812, United States
[h] University of Minnesota – Duluth, Department of Biology, 1303 Ordean Ct, Duluth, MN 55812, United States

ARTICLE INFO

Associate editor: Magdalena Osburn

Keywords:
Deep biosphere
STXM
S cycle
Fe cycle
Iron sulfide

ABSTRACT

The deep continental biosphere is supported by chemolithoautotrophy and depends on rock-derived substrates for energy. The majority of microorganisms in these crustal environments are likely attached to mineral surfaces within rock fractures, making characterization of deep life challenging. To better understand both biogeochemical cycling and mineral-hosted microbial communities in the deep subsurface, we characterized naturally occurring mineral particulate and associated biomass collected from boreholes drilled into a 2.7 Ga banded iron formation within the southern Canadian Shield. Particulate mineralogy was characterized via X-ray diffraction and Fe X-ray absorption near edge structure (XANES) spectroscopy. The particulate in one borehole was identified as a mixture of hematite and quartz, while the other borehole contained a mixture of the iron sulfides mackinawite and greigite, suggesting an active sulfur cycle mediated by microbial activity. Carbon associated with the particulate was imaged via scanning transmission X-ray microscopy and characterized via C XANES spectroscopy. In both boreholes, the particulate was colonized by microbial cells; many samples contained abundant biofilm. The cells and biofilm were chemically distinct, with the C XANES spectra for the cells consisting primarily of a protein-like signal and the biofilm resembling a mixture of protein, saccharide, and lipid. In the borehole containing the sulfidic particulate, the abundance of cells and biofilm increased with sample depth. Mineral particulate found in boreholes, whether forming *in situ* or as a result of drilling and weathering, are a valuable way to access the deep subsurface without the contamination and disturbance caused by drilling new cores. To better understand the microbial community composition and function associated with the particulate-biofilm aggregates and surrounding groundwater, filtered-water and particulate samples were characterized via shotgun metagenomic sequencing. Metagenomic analyses showed that while microbial communities were distinct between boreholes, all communities contained the genetic potential for the oxidation and reduction of a variety of sulfur phases. This suggests that the biogeochemical cycling of S, potentially connected to Fe cycling in this iron-rich habitat, could be fueling life in deep crustal environments.

* Corresponding author.
E-mail addresses: schu4222@umn.edu (C.J. Schuler), patsi005@umn.edu (A. Patsis), alexa017@umn.edu (S.C. Alexander), hsu00002@umn.edu (D. Hsu), lee02042@umn.edu (W. Lee), smatzen@umn.edu (S.L. Matzen), mamarcus@lbl.gov (M.A. Marcus), cssheik@d.umn.edu (C.S. Sheik), jill.mcdermott@lehigh.edu (J.M. McDermott), pkkang@umn.edu (P.K. Kang), santelli@umn.edu (C.M. Santelli), toner@umn.edu (B.M. Toner).
[1] Present address: Darcy Solutions, 5451 Zumbra Cir. Excelsior, MN 55331, United States.

https://doi.org/10.1016/j.gca.2024.04.019
Received 15 August 2023; Accepted 12 April 2024
Available online 16 April 2024

1. Introduction

Deep subsurface environments sustain a substantial portion of life on Earth – the continental crust in particular is estimated to contain 4–100 Pg carbon, potentially more than 20 % of Earth's total prokaryotic biomass (McMahon and Parnell, 2014; Magnabosco et al., 2018a). In the continental crust, microbial ecosystems are contained within water-filled fractures and pores. Fractures are of particular importance to deep subsurface environments, as they have significantly higher permeability than their host rock and allow for greater fluid flow. These environments are generally cut off from surface recharge over long timescales due to their depth; by the time waters reach the subsurface, they have been stripped of their oxygen and photosynthetically derived organic carbon (Lovley and Chapelle, 1995; Ferguson et al., 2023). While subsurface communities can contain diverse microbial communities including fermentative heterotrophs, these environments are sustained at a base level by chemolithoautotrophic organisms who derive energy and fix carbon by transforming inorganic substrates sourced from interactions between the surrounding water and rock (Stevens and Mckinley, 1995; Lin et al., 2006; Wu et al., 2016; Kieft et al., 2018). Studying the geochemistry of these crystalline, subsurface environments is essential to understanding the ecology and physiology of crustal microbial communities as well as the feedback between the geosphere, hydrosphere, and biosphere.

Because of their abundance in crustal environments, redox-active elements like iron and sulfur are expected to be essential sources of energy to support chemolithotrophic metabolisms in the subsurface (Pedersen, 1997; Lin et al., 2006; Bell et al., 2020; Casar et al., 2021). In anoxic environments, ferric iron minerals can serve as terminal electron acceptors to fuel Fe(III)-reducing metabolisms. These Fe(III)-reducing microbes cause the dissolution of iron (oxyhydr)oxide minerals and increase the concentration of soluble ferrous iron in many deep anoxic groundwaters (Lovley et al., 1991). Oxidized sulfur forms such as dissolved sulfate can also serve as terminal electron acceptors to fuel microbial metabolisms under reducing conditions (Muyzer and Stams, 2008). Sulfate can be abundant in many subsurface environments, in part due to the dissolution of sulfate-bearing minerals such as gypsum and anhydrite and the oxidation of sulfide minerals like pyrite (Fritz and Frape, 1982; Fritz et al., 1994; Li et al., 2016). Sulfur-reducing microorganisms that reduce sulfate to sulfide are some of the most frequently observed microbes in anoxic subsurface environments (Olson et al., 1981; Stevens and Mckinley, 1995; Krumholz et al., 1997; Haveman et al., 1999; Baker et al., 2003).

The traditional "redox ladder" described in anaerobic environments suggests that after all ferric iron is reduced, microbial sulfate reduction will dominate in these environments until the pool of oxidized sulfur is consumed. There is also evidence, however, of a more complex anaerobic sulfur cycle that expands beyond the ubiquitous microbially-driven sulfate reduction and involves both sulfur reduction and subsequent oxidation through both abiotic and biotic processes linked to Fe(III) or nitrate reduction (Elsgaard and Jørgensen, 1992; Canfield et al., 2010; Holmkvist et al., 2011). Iron (oxyhydr)oxide minerals and organically complexed Fe(III) can oxidize microbially produced sulfide, catalyzing the formation of sulfur intermediates such as elemental sulfur (S^0) and thiosulfate ($S_2O_3^{2-}$) (Pyzik and Sommer, 1981; Luther et al., 1992; Poulton et al., 2004). These sulfur intermediates can be further oxidized, reduced, or disproportionated through abiotic or biotic reactions. These reactions prevent the buildup of reduced sulfur compounds and drive the biogeochemical sulfur cycle forward. "Cryptic" sulfur cycles can be hard to detect; sulfate and sulfide concentrations can stay relatively stable due to the consistent rates of reduction and oxidation, and many intermediate sulfur forms are difficult to detect in environmental settings as they are unstable under most conditions and frequently exist at low concentrations (Holmkvist et al., 2011). To shed light on these linked biogeochemical iron and sulfur cycles, researchers have combined geochemical analyses with incubation experiments to determine the rate of microbial sulfur reduction or with genomic sequencing to look at a microbial community's metabolic potential for iron and sulfur cycling (Holmkvist et al., 2011; Pellerin et al., 2018; Ng et al., 2020). Recent metatranscriptomic and metaproteomic studies of the deep continental subsurface have shown that both sulfur-reducing microorganisms and sulfur-oxidizing microorganisms can be active in the same environment (Lau et al., 2016; Bell et al., 2020). While cryptic sulfur cycles have primarily been described in deep marine sediments, further research is needed to resolve their activity and biogeochemical impact in deep continental environments where iron oxides are present in host rock and may fuel the abiotic oxidation of sulfide.

There are also outstanding questions about the deep continental biosphere pertaining to the differences between microbes attached to rock fracture surfaces and those in free-floating planktonic communities. Most microbes in these fractured-rock environments are expected to be attached to rock surfaces or in biofilms (Lehman et al., 2001; Flemming and Wuertz, 2019). Because researchers commonly access the subsurface through sampling groundwater in boreholes, the majority of studies of these subsurface environments have focused on planktonic populations, e.g. (Kieft et al., 2005; Moser et al., 2005; Lin et al., 2006; Onstott et al., 2009; Itävaara et al., 2011). These studies are important and have advanced our understanding of the biogeochemical dynamics of subsurface environments. There remains, however, a great deal of uncertainty in the ratio of surface-attached versus planktonic cells, leading to order-of-magnitude level differences in estimates of total cells and biomass in the subsurface (McMahon and Parnell, 2014). Additionally, major differences in the composition of surface-attached and planktonic microbial communities have been observed in both laboratory and field-based incubation experiments (Lehman et al., 2001; Jones and Bennett, 2017; Wu et al., 2017; Casar et al., 2020; Nuppunen-Puputti et al., 2021). Because of this, focusing solely on groundwater-hosted, planktonic populations (and incubation experiments using groundwaters and their associated microbes) could lead to major gaps in our knowledge of subsurface communities. The lack of published studies focusing on surface-attached subsurface microbial communities stems in part from the difficulties involved in retrieving intact, useful samples. Accessing crustal environments requires drilling; this process can destroy fragile biomaterials through abrasion, and mud or water pumped in during the drilling process can introduce contamination (Santelli et al., 2010). Careful drilling has allowed for studies of attached microbial communities and biofilms on fracture surfaces (Escudero et al., 2018). In many studies of rock-hosted microbial communities, however, the outer portions of rock cores were discarded or sterilized due to potential contamination, eliminating the bulk of the surface-hosted community and focusing instead on lower-abundance pore-hosted microbes (Momper et al., 2017b; Dutta et al., 2019). New approaches for accessing surface- and biofilm-attached microbial communities and resolving their geochemical imprint in subsurface environments are needed to continue advancing our understanding of deep subsurface life.

The Soudan Underground Mine State Park, located in Soudan, Minnesota (MN), USA, provides a natural laboratory for the investigation of iron and sulfur cycling in groundwater and surface-attached microbial communities in the deep continental subsurface. This site accesses deep, isolated groundwaters in fractured Archaean rocks and has been the subject of previous research into the deep biosphere (Edwards et al., 2006; Sheik et al., 2021; Dowd et al., 2022; Schuler et al., 2022). The Soudan formation, accessed by legacy subsurface boreholes in the mine, contains both banded iron formation (BIF) rich in iron oxides and schistose regions free of iron oxides (Peterson and Patelke, 2003; Schuler et al., 2022). Thus, fractures intersecting differing lithologies at this site may reach waters with divergent processes affecting iron and sulfur cycles. The walls of boreholes at this site were found to be coated in mm to cm thick layers of mineral particulate; borehole waters also contained suspended mineral aggregates. This particulate provides a mineral-rich substrate that could be sampled without new drilling, avoiding the common risks of the contamination or destruction of surface-hosted

microbial communities. This paper characterizes mineral particulate samples collected from subsurface boreholes. The mineralogy and morphology of the retrieved particulate was characterized using X-ray diffraction (XRD), scanning electron microscopy (SEM), scanning transmission X-ray microscopy (STXM), and Fe X-ray absorption near edge structure (XANES) spectroscopy to better understand the biogeochemical processes forming these secondary mineral phases. Particulate mineralogy was used in combination with the rock and water chemistry at the Soudan Mine to expand our understanding of subsurface iron and sulfur cycles. Organic carbon associated with the minerals was characterized using SEM, STXM, and C XANES spectroscopy to explore microbial colonization and biofilm formation. This geochemical data was augmented with genomic data through the extraction and sequencing of DNA from both groundwater samples and a particulate sample. Metagenomes were assembled for these samples to describe the microbial community and its potential for the biogeochemical cycling of iron and sulfur. Understanding the microbial and geochemical dynamics of the deep continental biosphere is important because these environments host a significant proportion of the prokaryotic life on Earth (McMahon and Parnell, 2014; Magnabosco et al., 2018a) and have been proposed as storage sites for hydrogen and for pollutants such as carbon dioxide and nuclear waste (Holloway, 1997; Gascoyne, 2004; Heinemann et al., 2021). This study expands our understanding of the biogeochemical cycling of iron and sulfur within fractured-rock hosted groundwaters and points to subsurface particulate like that found in the Soudan boreholes as important avenues for exploring microbial community structure in the continental subsurface.

2. Methods

2.1. Field Site

Samples were collected at the Soudan Underground Mine State Park (Soudan Mine), located in Soudan, MN, USA. This site is located within the Canadian Shield and allows access to a 2.7 Ga BIF and isolated groundwaters (Fig. 1) (Cloud et al., 1965; Schuler et al., 2022). Though the precise residence times of these groundwaters have not been determined, other waters in the Canadian Shield with comparable depth and salinity have residence times on the order of 10–100 Ma (Warr et al., 2021; Ferguson et al., 2023). The Soudan Mine was an active iron mine until 1962; it has been continually managed by the Minnesota Department of Natural Resources (MN DNR) since. The MN DNR pumps water from the mine, preventing flooding from either ground or surface water. Samples were collected from boreholes on the west drift of the mine's deepest level, the 27th, which is over 700 m below the surface. The boreholes sampled in this study, diamond drill holes 932, 944, and 951 (Fig. 2), were drilled between the years 1958–1960 (Klinger, 1958; Bakkila, 1960a,b). All three boreholes were drilled at a downward angle into the Soudan Formation. This formation contains the 2.7 Ga hematite-jasper-chert BIF as well as pockets of massive hematite ore, chlorite schist, and chlorite-sericite schist (Peterson and Patelke, 2003; Schuler et al., 2022). The boreholes tap into subsurface fracture networks hosting an anoxic calcium-sodium-chloride brine with total dissolved solids (TDS) concentrations ranging from 76,000–116,000 mg/L, characteristic of deep groundwaters across the Canadian Shield (Frape et al., 1984; Schuler et al., 2022). The boreholes have had continuous positive pressure flow since drilling with flow rates ranging from 1.1–3.4 mL/

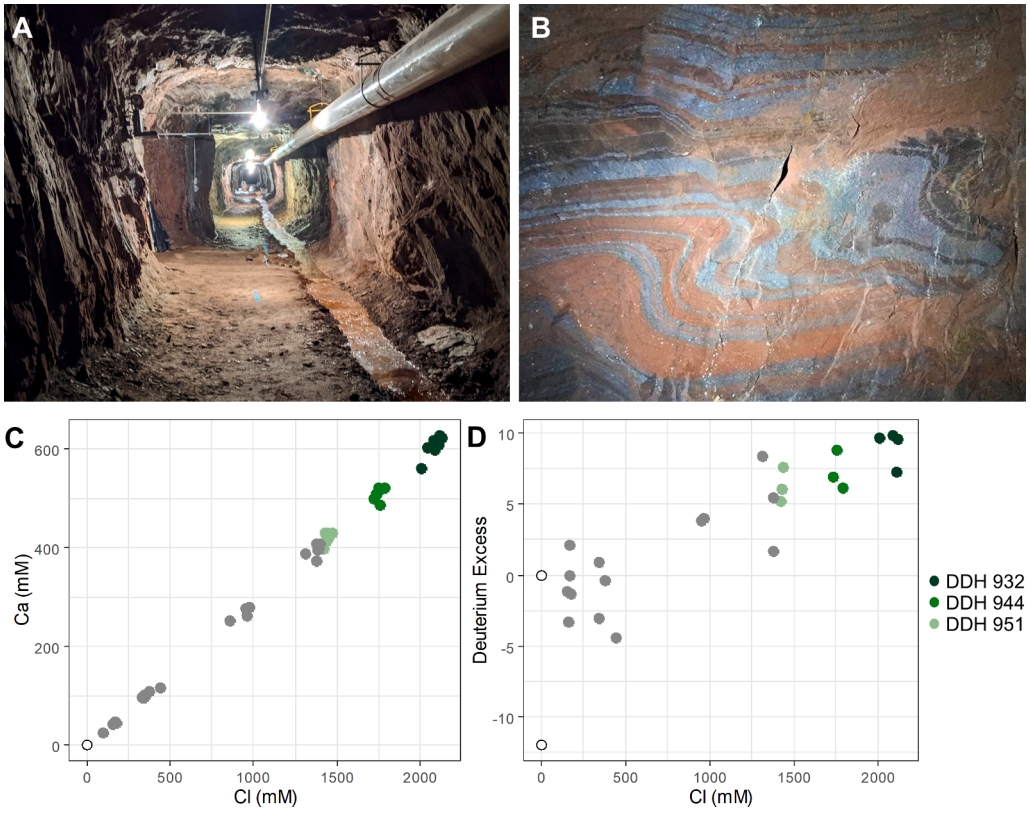

Fig. 1. A. The west drift of the 27th level of the Soudan Underground Mine State Park, where the samples for this study were collected. B. The banded iron formation accessed by the west drift of the Soudan Mine. C. Chloride versus calcium concentrations for Soudan groundwaters from a previous study highlighting broader trends in water chemistry (Schuler et al., 2022) – calcium scales linearly with chloride, showing that all boreholes derive their salinity from a single Source. D. Chloride concentrations versus deuterium excess for Soudan groundwaters (Schuler et al., 2022), showing that the most saline groundwaters are also the most isolated from surface inputs. The colors corresponding to boreholes discussed in this paper are indicated on the figure, while gray points indicate samples from other boreholes at Soudan and the hollow black points indicate surface waters from a nearby lake.

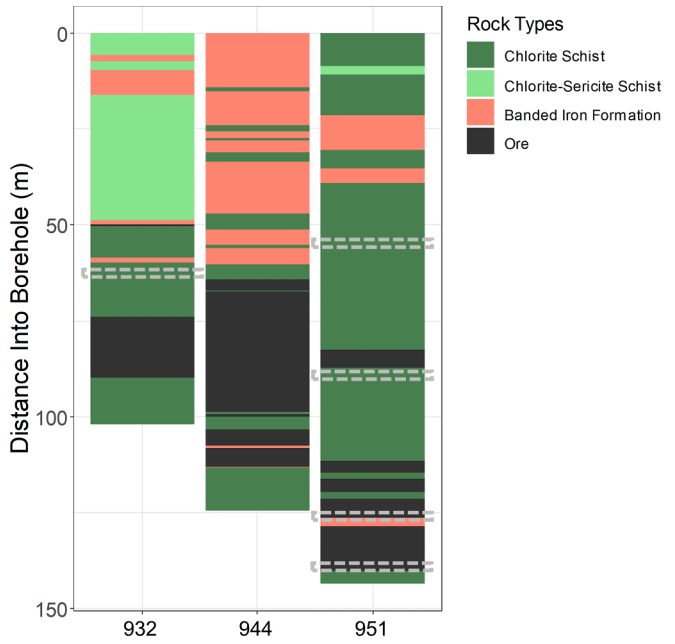

Fig. 2. Lithologic profiles of rock cores from boreholes 932, 944, and 951 adapted from (Schuler et al., 2022). Mineral precipitate sampling locations are indicated by dashed gray boxes. Genomic samples were collected roughly one meter below the mouths of the borehole. Lithologies at depth were determined by consulting borehole cores and drillers notes as described previously (Schuler et al., 2022).

min (Dowd et al., 2022). Boreholes have steady geochemical, hydraulic, and microbiological characteristics, allowing spatial trends within the mine to be evaluated. Several boreholes contain fine-grained mineral particulate. This particulate coated the borehole walls and at some depths was thick enough to partially or fully block the borehole passage.

2.2. Particulate Chemistry

2.2.1. Sample Collection

Mineral particulate was collected from specific borehole depths using a sampling system composed of a high-volume peristaltic pump (Golander Pump) and 2.13 cm diameter flush-threaded PVC tremie pipe in 3.05 m sections (Johnson Screens). Tremie pipe was cleaned and sterilized on both the inside and outside using 70 % ethanol prior to insertion into the borehole. Water and particulate were pumped from a given depth and collected in 30 mL glass vials with Teflon-lined serum caps. Samples were collected in boreholes 932 and 951 (Table 1, Fig. 2). Samples for electron microscopy were spiked with paraformaldehyde to bring the total paraformaldehyde concentration in the vials to 2.5 % v/v. The headspace in the vials was flushed with N_2 gas for 60 s; the samples were then sealed in mylar bags along with AnaeroPaks (Mitsubishi Gas Chemical Co.) to scrub oxygen from the storage bag and ensure anoxic conditions for storage. Samples were stored at 4 °C until ready for analysis.

Table 1
Temporal and spatial information for particulate geochemistry samples.

Borehole	Sampling Depth (m into borehole)	Sampling date (dd/mm/yyyy)	Primary Lithology at Sampling Depth
932	64	28/06/2019	Chlorite schist
951	56	26/06/2019	Chlorite schist
	90	15/11/2019	Chlorite schist
	126	15/11/2019	Ore/Banded Iron Formation
	139	15/11/2019	Ore

2.2.2. X-ray diffraction

Samples were opened in an anaerobic chamber filled with a mixture of 95 % N_2 and 5 % H_2 and collected onto 0.2 μm polycarbonate filter membranes (Poretics) via vacuum filtration. Samples were then rinsed three times using N_2-sparged Milli-Q water to remove salts. These membranes were mounted onto XRD sample holders and sealed using Kapton tape (Bertech). The prepared samples were resealed in mylar until ready for analysis. In addition to the samples, a blank filter was also measured for use in background correction. Samples were analyzed at the Characterization Facility of the University of Minnesota using a Bruker D8 Discover diffractometer. The sample from borehole 932 and the 56 m sample from borehole 951 were analyzed with a Cu Kα radiation source; the other three samples from borehole 951 were analyzed with a Co Kα radiation source. Diffraction patterns were processed using Match! software (version 3.13) and the PDF-4 diffraction database (Putz and Brandenburg, 2003).

2.2.3. Electron Microscopy

Mineral particulate samples were prepared and washed as described above in section 2.2.2, then dehydrated using a series of ethanol solutions with increasing concentrations (30 %, 50 %, 70 %, 80 %, 90 %, 95 %, 100 %, 100 %, 100 %) with the solutions changed in ten-minute intervals. The filters were cut to the size of the sample holder using a razor blade and mounted on carbon tape. Samples were coated with 7.5 nm Pt using a VCR Group Incorporated IBS/TM200S Ion Beam Sputterer prior to imaging. Samples were imaged with an operating voltage of 2 kV at the Characterization Facility of the University of Minnesota using a FEI Helios NanoLab G4 Scanning Electron Microscope.

2.2.4. Scanning Transmission X-ray Microscopy

Mineral particulate samples were prepared and washed as described in *2.2.2 X-ray Diffraction*, then transferred into a microcentrifuge tube and resuspended in N_2-sparged Milli-Q water. This suspension was deposited onto a silicon–nitride (Si_3N_4) membrane (Silson Ltd.) and allowed to dry under N_2 gas (Toner et al., 2016). In cases where the particulate deposited from the original suspension was too thick for analysis, suspensions were diluted ten-fold or hundred-fold with N_2-sparged water and new membranes were prepared with the diluted suspension. Prepared membranes were sealed in N_2-filled mylar pouches and stored at 4 °C until ready for analysis.

Scanning transmission X-ray microscopy (STXM) was performed at beamline 5.3.2.2 at the Advanced Light Source in Berkeley, CA (Kilcoyne et al., 2003). Samples were imaged and XANES spectra were collected at the carbon 1 s and iron 2p edges. Sample analysis was conducted in a helium-flushed microscope chamber. X-ray intensity was measured in transmission mode using a scintillator-photomultiplier detector assembly. For carbon spectroscopy, the monochromator was calibrated using the Rydberg transitions of gaseous carbon dioxide at 292.74 and 294.96 eV. For iron spectroscopy, the monochromator was calibrated using a ferrihydrite standard with the main peak of the Fe 2p spectrum set to 709.5 eV.

Data consists of three distinct types: (1) transmission "images" at a single X-ray energy, (2) optical density elemental "maps" prepared from images taken below and above the X-ray edge for an element of interest, and (3) image "stacks" taken at incremental energy steps spanning the absorption edge of the element of interest. Maps and stacks were processed using STXM Image Reader (Marcus, 2022). Maps were generated using the difference in pixel intensity between the below-edge and above-edge energy measurements. XANES spectra were extracted from image stacks by grouping similar pixels into clusters using principal component analysis, then summing X-ray absorbance across a cluster of similar pixels. XANES spectra were background corrected and normalized using the software axis2000 (version 2021_07_06) (Hitchcock, 2021). Spectra were grouped according to the morphology of the cluster from which they were extracted. For the C XANES spectra, clusters were categorized as cells, which resembled rods, cocci, or filaments, films,

which had a tufted texture and resembled extracellular polymeric substance (EPS) or biofilm, or background, with background spectra coming from locations on the membrane with no sample. For the Fe XANES spectra, clusters were categorized as particulate, film-associated, or background. For both sets of XANES spectra, the background spectra were discarded, and the remaining spectra were compared to C and Fe reference spectra. The C published reference spectra were alginate, a saccharide, bovine serum albumin protein (BSA), deoxyribonucleic acid (DNA), lipid, and calcium carbonate ($CaCO_3$); they have previously been published (Toner et al., 2009; Hoffman et al., 2018). The Fe standards were iron monosulfide (FeS), ferrihydrite ($Fe_{10}O_{14}(OH)_2$, see (Michel et al., 2007)), pyrite (FeS_2), and pyrrhotite ($Fe_{0.8\text{-}1.0}S$). The iron monosulfide was synthesized according to the method described in (Butler and Hayes, 1998), while the other iron standards were previously published (Toner et al., 2009).

2.3. Rock Chemistry

Thin sections were prepared from rock cores collected in 1958 and stored at the Soudan Mine. The mineralogy of these cores has been described elsewhere (Schuler et al., 2022). Rock fragments for thin sections were selected from depth increments near active fracture sites. Specifically, core segments with visible weathering or alteration phases and depth correlation with apparent fractures in down-borehole camera footage were selected. Thin sections were prepared by Spectrum Petrographics Inc. in Vancouver, WA. Samples were fixed in epoxy, sectioned, prepared with a double-side microprobe quality polish to a final thickness of 30 μm, and mounted with cyanoacrylate glue to Suprasil 2A Quartz glass (the "combined synchrotron XRF/XRD" preparation). Thin section analysis included petrographic light microscopy, electron microscopy, and synchrotron-based X-ray microprobe.

Thin sections were prepared for electron microscopy by sputter-coating with carbon using a Leica ACE600 to a final thickness of 10 nm. Electron Microprobe Analysis (EMPA) was conducted at the University of Minnesota using a JEOL JXA-8530FPlus Electron Probe Microanalyzer. Images were collected with an accelerating voltage of 15 keV and a current of 10nA.

X-ray microprobe analysis of the thin sections was performed at beamline 4-BM at the National Synchrotron Light Source – II (NSLS-II) in Upton, NY. Instrument monochromators were calibrated at the Fe 1 s edge using a metallic iron foil and at the As 1 s edge using the white-line peak of As(V) in a topaz sample. Fluorescence was measured using a Vortex-ME7 silicon drift detector (Hitachi). Coarse-resolution X-ray fluorescence (XRF) maps were collected using a beam diameter of 9 μm and a step size of 10 μm. Fine-resolution XRF maps were collected using a beam diameter of 5 μm and a step size of 5 μm. All XRF maps were collected with a dwell time of 0.05 s. XRF maps were collected at two energies: 6640 eV (below the Fe 1 s edge) and 12500 eV (above the As 1 s edge). XRF map data was analyzed using the GSE Map Viewer program, part of the Larch software package (Newville, 2013). μ-XRD patterns was collected using a XRD 1621 N ES amorphous silicon digital X-ray detector (PerkinElmer). Diffraction patterns were measured in transmission mode, through the quartz slide, using a beam energy of 18000 eV and a dwell time of 60 s. The diffraction data were processed by masking the primary beam stop, subtracting the background diffraction from the quartz slide, and radially integrating the measured diffraction pattern to convert the two-dimensional diffraction images into one-dimensional diffraction intensity patterns. The computer program Dioptas was used for diffraction data processing (Prescher and Prakapenka, 2015). The resulting diffraction patterns were analyzed as described in *2.2.2 X-ray Diffraction*.

2.4. Community Genomics

2.4.1. Sample Collection, DNA Extraction, and Sequencing

Samples were collected for the extraction of DNA from water and mineral particulate (Table 2). Water samples were collected by pumping water from the boreholes using a peristaltic pump (Cole-Parmer). To access deeper waters, a half-meter sterile copper tube attached to autoclaved platinum-cured silicone tubing (Masterflex) was placed into the boreholes. Borehole fluids were filtered through sterile 0.22 μm polyvinylidene fluoride Sterivex filter units (Millipore) for four hours or until the filters clogged, with an estimated 2.5 L filtered per sample. Mixed particulate-water samples were collected from the borehole using sterilized PVC tremie piping in the same manner as those for chemical analyses. Mineral particulate was pumped from within the borehole as described in *2.2.1 Sample Collection* and filtered through a Sterivex filter unit, with 60 mL of a mineral–water mixture pumped through the filter. Filters were immediately frozen on dry ice and stored at −80 °C until ready for analysis.

Immediately prior to extraction, the filter was removed from the outer cartridge in a laminar flow hood. DNA was extracted from the filter using a FastDNA Spin Kit for Soil (MP Biomedicals). The extraction procedure followed the kit instructions but used the following recommended enhancements for low-DNA systems: samples were homogenized twice to improve mechanical lysis, and the elution buffer and DNA binding matrix were incubated at 55 °C for 5 min prior to the final elution of DNA. Extracts were quantified using a Qubit 2.0 fluorometer (ThermoFisher Scientific) and the Qubit broad-range assay kit. Extracts with sufficient DNA were sent to the University of Minnesota Genomic Center for sequencing. Extraction kits with no sample were used as a negative control to check for contamination; no sequences were recovered from these blanks. Dual-indexed libraries were generated using the Illumina DNA Prep workflow (Illumina Document #1000000025416 v09) and sequenced on the Illumina NextSeq 6000 platform in one lane of a 2x150 base pair run. The mean quality scores for all libraries were greater than or equal to Q30.

2.4.2. Metagenome Processing, Binning, and Analysis

Prior to assembly, sequences were trimmed and filtered for length and quality using FastP v. 0.23.2 under the default parameters (Q20) with base correction (Chen et al., 2018). Reads were assembled using metaSPAdes v. 3.15.4 under the default parameters (Nurk et al., 2017). Scaffolds were then binned into metagenome assembled genomes (MAGs) using the binning module of MetaWrap v. 0.0.2 (Uritskiy et al., 2018). Initial bins were extracted using both CONCOCT v 1.10 and the MetaBAT1 and MetaBAT2 algorithms within MetaBAT2 v 2.15 (Alneberg et al., 2014; Kang et al., 2019). The bins were deduplicated and aggregated with DAS Tool v. 1.1.3 (Sieber et al., 2018). The genomes were assessed for completeness and quality using CheckM2 version 0.1.3 and for coverage using CoverM v. 0.6.1 (Woodcroft, 2021; Chklovski et al., 2022). Taxonomic assignments were determined using the classify_wf tool in GTDB-Tk v. 2.1.1 and the Genome Taxonomy Database (release r207 v2) (Chaumeil et al., 2022).

The genetic potential of reconstructed genomes was determined

Table 2
Sample locations, names, and collection dates for genomic samples. All filtered water samples were collected 0.5 m below the entrance to the borehole, while the mineral particulate sample was collected 56 m below the entrance of the borehole. [a]Data from these samples were previously published (Sheik et al., 2021). [b]Collected after clearing debris from the entrance to the borehole.

Borehole	Sample Name	Sampling Date	Sample Type
932	W-2014-932	2014	Filtered water[a]
	W-2019-Pre-932	22/02/2019	Filtered water
	W-2019-Post-932	25/02/2019	Filtered water[b]
944	W-2014-944	2014	Filtered water[a]
	W-2019-944	25/02/2019	Filtered water
	W-2021-944	21/10/2021	Filtered water
951	W-2014-951	2014	Filtered water[a]
	W-2019-951	25/02/2019	Filtered water
	P-2019-951	26/06/2019	Mineral particulate

using METABOLIC v. 4, which uses a comprehensive database to search for key metabolic marker genes of interest (Zhou et al., 2022). Marker genes for iron metabolisms were also predicted using the FeGenie bioinformatics tool version 1.0 (Garber et al., 2020). The MMseqs2-based fast.genomics tool was used to supplement the FeGenie predictions with homology validation (Price, 2023). Indicator species analysis was performed to identify associations between specific taxa and sampling locations using the "multipatt" function in the R package "indicspecies" (De Cáceres and Legendre, 2009). Patterns in microbial community composition across boreholes were analyzed based on Bray-Curtis dissimilarity matrices of relative microbial abundance and visualized by non-metric multidimensional scaling (NMDS). These analyses were conducted using the *metaMDS* function in the "vegan" package of R.

3. Results

3.1. Mineral Particulate Properties

3.1.1. Field Observations

During sample collection, the overall distribution and characteristics of mineral particulate at different depths were noted for boreholes 932 and 951. The particulate sampled at each depth is likely a combination of materials suspended in brine and settled on the borehole wall. The particulate in borehole 932 was red in color throughout the borehole. Upon collection, the particulate was a mixture of fine particles that remained suspended in water for minutes or longer and larger particles that settled out of solution on the order of seconds or tens of seconds. Particulate was first visible in water samples from borehole 932 at a depth of 12 m below the borehole opening. The amount of particulate drawn up along with the borehole water increased at depths greater than 43 m, and the borehole became fully blocked by particulate at a depth of 69 m, so sampling was discontinued after that depth. In borehole 951, the particulate was consistently black in color. Particulate was first visible in water samples at a depth of 50 m; at these shallower depths, the particulate solely consisted of fine particles with an oily appearance in aggregate. The overall size of particles in the sample based on visual inspection began to increase with depth starting at 125 m into the borehole. Although not quantitatively measured, the volume of particulate relative to overall sample volume also visibly increased with depth – appreciable increases specifically occurred at 80 m, 125 m, 135 m, and 145 m. Borehole 951 never became fully blocked by particulate and the full reported depth was accessed.

3.1.2. Bulk Particulate Mineralogy

Powder XRD revealed that the particulate from borehole 932 contained hematite (Fe_2O_3) and quartz (SiO_2) (Figure S4). Overall, the diffraction peaks from this sample were of greater intensity than the peaks obtained from any of the borehole 951 particulate samples. All four particulate samples from borehole 951 contained a mixture of mackinawite (FeS), the mixed-valence iron sulfide greigite (Fe_3S_4), and quartz. The shallowest sample (from 56 m) had the most intense diffraction peaks and the mackinawite signal in this sample seemed to be stronger than the greigite signal (Figure S5). In the three deeper samples (from 90, 126, and 139 m), the overall diffraction intensity was much weaker (Figure S6). The relative contributions to the overall pattern from mackinawite and greigite seemed to differ from sample to sample, with the relative greigite intensity being greater in the shallower samples and the relative mackinawite intensity being greater in the deeper samples.

3.1.3. Microscopy

The samples were imaged using both SEM and STXM. These two methods provide complementary morphological information. SEM allows for the imaging of whole particle aggregates, provides a greater depth of field, and shows surface textures. Because STXM images are measured in transmission mode, these images have no depth of field; however, STXM allows for the determination of the size, shape, and elemental composition of single particles as well as the mapping of the distribution of elements and chemical species throughout samples.

When imaged by SEM (Fig. 3) and STXM (Fig. 4), the particulate in borehole 932 had two distinct mineral phases with variable grain size and shape. The largest grains were up to 60 μm in diameter, most were between 5–25 μm, and some were smaller than 1 μm. One set of mineral grains had uneven fracture and anhedral grains; under the STXM, these grains contained iron (Fig. 4B). They were likely hematite as identified by XRD. The other set of mineral grains had conchoidal fracture and more well-defined crystal faces; these grains contained neither iron nor carbon and were likely quartz. In addition to the mineral grains, the particles were associated with several distinct carbon-bearing morphotypes (Fig. 4C). One of these was consistent with microbial cells: 1–2 μm long rod and coccus shaped cells and filamentous cells with a length of 4 μm or greater. The other carbon-bearing morphotype resembled biofilm or EPS. When imaged via SEM, the film morphology had a smoother, less jagged surface than the surrounding mineral grains. When imaged via STXM, it resembled tufts or whisps, had a lower optical density than the surrounding minerals or cells, and was composed of organic C (see *3.2.1 Carbon XANES*).

The particulate in borehole 951 had three distinct types of non-carbonaceous particles (Fig. 3, Fig. 5). Two of these contained iron based on STXM. One set of particles was primarily composed of bladed rosettes and thin sheets (Fig. 3D) characteristic of mackinawite (Herbert et al., 1998; Csákberényi-Malasics et al., 2012). Another set of particles contained a mixture of thicker plates and cubo-octahedral grains (Fig. 3B), these were likely greigite (Horiuchi et al., 1974; Chang et al., 2008). Overall, the relative abundance of greigite seemed to decrease with depth. A third set of grains with irregular features and conchoidal fracture could also be seen, features associated with quartz. The largest grains were over 10 μm across; most were between 1–2 μm, and the smallest particles were less than 500 nm across. The carbonaceous cell and film morphotypes seen in the sample from borehole 932 were also observed in all particulate samples from borehole 951. Cells and film were less abundant in the shallower samples (56 and 90 m), but the two deeper samples (126 and 139 m) contained abundant cells with diverse morphologies including rods, cocci, filaments, and spores. Most mineral grains from these deeper samples also had associated EPS, while some grains had dense biofilms covered in numerous cells (Fig. 3C).

3.2. XANES Analysis

3.2.1. Carbon XANES

Carbon XANES spectra were collected via STXM for cells and films. The spectra showed that these morphologies were chemically distinct. Carbon spectra from cells were collected from all samples except for the shallowest borehole 951 sample. The carbon spectra for cells were similar for all depths in both boreholes (Fig. 6, cell spectra) and confirmed the presence of proteins and lipids (materials present in microbial cells). All of these spectra had sharp peaks at 285.17 ± 0.06 and 288.3 ± 0.1 eV, peaks associated with C = C double bonds and carboxylic or carbonyl C = O bonds, respectively (Lehmann et al., 2009; Nico et al., 2017). Both of these peaks are commonly associated with proteinaceous carbon (Toner et al., 2009). All spectra had shoulders at 287.2 ± 0.2 eV, associated with aliphatic C–H bonding and commonly observed in lipids (Lehmann et al., 2009; Toner et al., 2009; Nico et al., 2017). In addition to the spectral features described above, 54 % of the spectra from cells had peaks at 289.5 ± 0.3 eV. Peaks in this region are associated with C-OH bonding in alcohols (Lehmann et al., 2009; Nico et al., 2017). Forty-five percent of the cell spectra had sharp peaks around 290.4 ± 0.2 eV, associated with C = O bonding in carbonate minerals and prominent in the calcite standard (Brandes et al., 2010; Nico et al., 2017).

Carbon spectra from films were collected from all samples. The carbon speciation was more heterogeneous for the films than for the

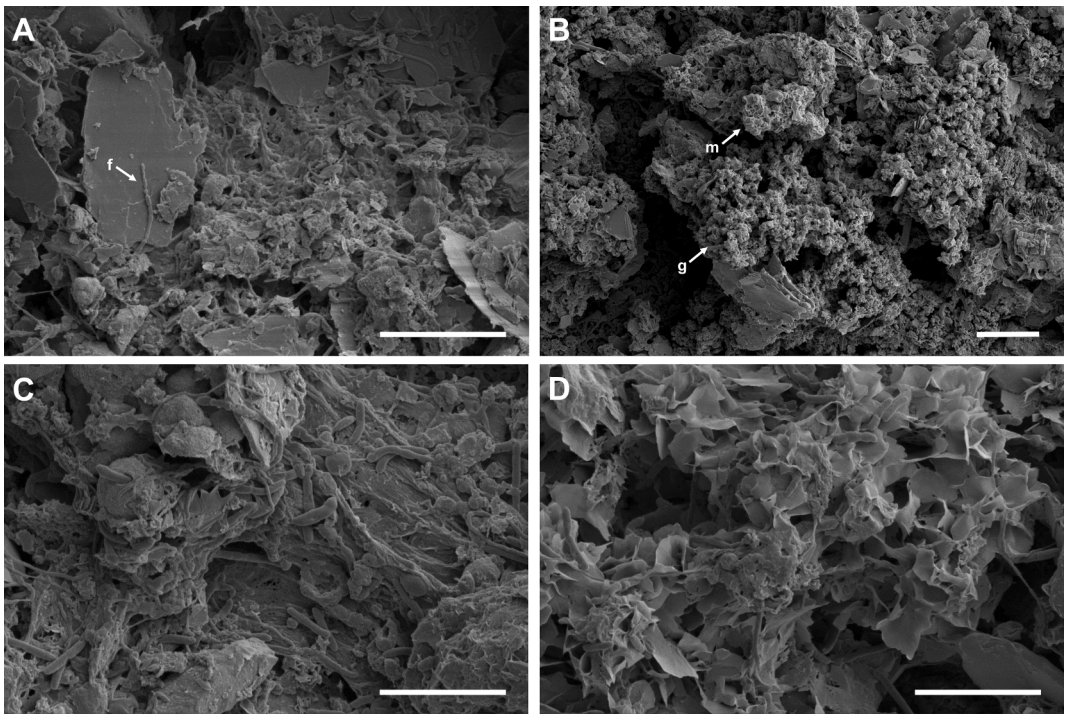

Fig. 3. SEM images of mineral particulate samples. A. Hematite and quartz grains from borehole 932 covered in a biofilm and colonized by filamentous microorganisms – an example cell is labeled "f". B. Particulate collected 56 m into borehole 951. Clusters of greigite plates and cubo-octahedral grains ("g") can be seen along with thinner mackinawite sheets ("m"). C. Mackinawite collected 139 m into borehole 951 covered in a thick biofilm and morphologically diverse cells (cocci, filaments, rods, etc.). D. Mackinawite rosette collected 139 m into borehole 951 consisting of large, thin sheets. All scale bars are 5 μm in length.

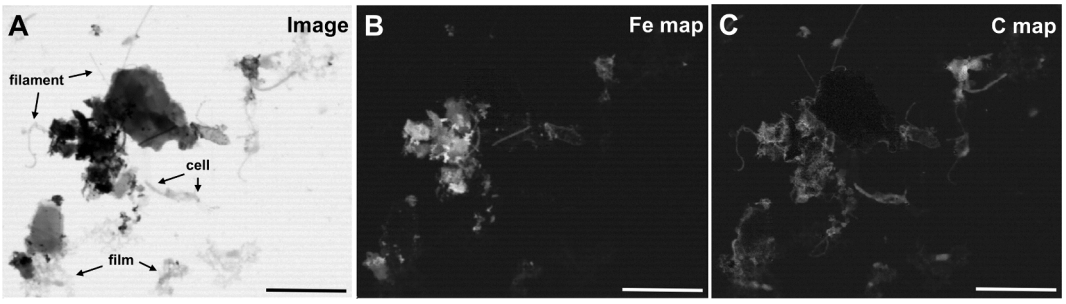

Fig. 4. A. Scanning transmission X-ray microscopy (STXM) image of borehole 932 particulate at 710 eV. Examples of films, cells, and filamentous cells are labeled. Darker pixels indicate lower X-ray transmission. B. Iron map of the same area as A prepared from STXM images below and above the iron 2p edge (700 and 710 eV) – brighter pixels indicate higher iron concentration. C. Carbon map of the same area as A prepared from STXM images below and above the carbon 1 s edge (280 and 290 eV) – brighter pixels indicate higher carbon concentration. All scale bars are 10 μm in length.

cells (Fig. 6, film spectra). Most spectra had peaks or shoulders at similar energy values, but the relative intensities of these peaks varied. Overall, the spectra resembled a mixture of biomolecules; protein-like and saccharide-like features were most prominent, but some spectra also resembled lipids and inorganic mineral carbon. All samples had sharp peaks at 285.19 ± 0.04 eV and 288.4 ± 0.2 eV, associated with C = C double bonds and carbonyl C = O bonds (Lehmann et al., 2009; Nico et al., 2017). These peaks likely result from the combination of protein-associated peaks, commonly observed at 288.2 eV, and saccharide-associated peaks, commonly observed at 288.6 eV (Chan et al., 2004; Benzerara et al., 2005). All of the spectra also had weak peaks or shoulders at 287.4 ± 0.3 eV, associated with aliphatic C–H bonding and commonly observed in lipids, and broad spectral features at 293.2 ± 0.7 eV, associated C–C sigma antibonding orbitals (Lehmann et al., 2009; Toner et al., 2009; Nico et al., 2017). Most spectra (86 %) had peaks or shoulders at 290.4 ± 0.2 eV, associated with carbonate C = O bonds (Brandes et al., 2010; Nico et al., 2017). Approximately half of the spectra (57 %) had peaks or shoulders at 289.8 ± 0.1 eV, associated with C-OH bonding in alcohols (Lehmann et al., 2009; Nico et al., 2017). Finally, some spectra (43 %) had sharp peaks at 297.3 ± 0.3 eV, associated with potassium's 2p X-ray absorption edge (Claret et al., 2002; Nico et al., 2017).

3.2.2. *Iron XANES*

As expected from visual observations and XRD analysis, the Fe XANES spectra from particulate from the two boreholes were distinct from one another (Fig. 7, particulate spectra). The spectra from borehole 932 resembled ferric iron, while the particulate spectra from borehole 951 resembled iron sulfide. The two spectra from borehole 932 particulate had the same features: a low-absorption peak or shoulder at 707.8 ± 0.1 eV, a strong, sharp peak at 709.33 ± 0.09 eV, and weak peaks at 721.0 ± 0.2 and 722.5 ± 0.1 eV. These spectral features are all consistent with Fe(III)-bearing phases. While ferrihydrite was used as a reference to describe the XANES spectra for ferric iron, distinguishing between different iron (oxyhydr)oxides using XANES spectra from the iron 2p edge is often impossible (Toner et al., 2009). The spectra from all

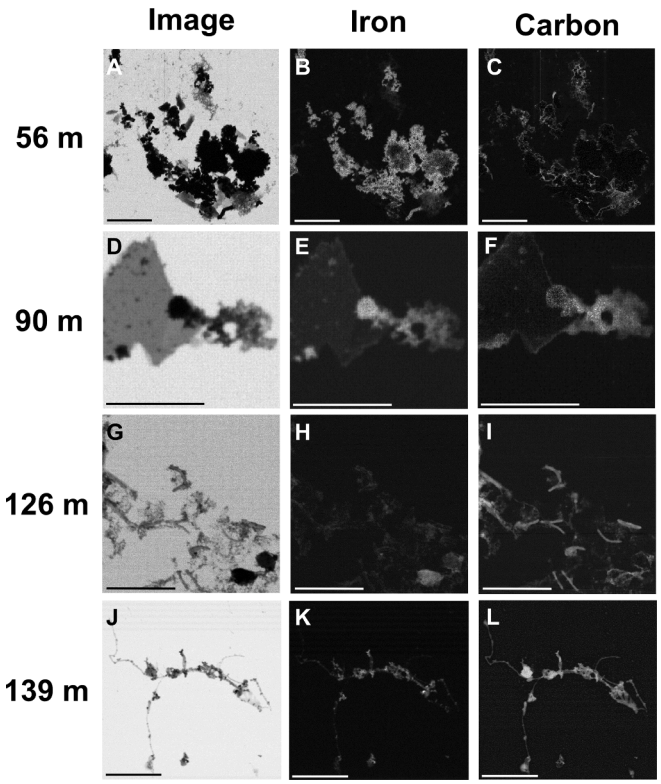

Fig. 5. Scanning transmission X-ray microscopy (STXM) images and optical density maps of particulate from borehole 951. Samples were collected at 56 m (A – C), 90 m (D – F), 126 m (G – I), and 139 m (J – L) into the borehole. The first column (A, D, G, J) contains transmission images taken above the Fe edge at 710 eV – darker pixels indicate lower X-ray transmission. The second column (B, E, H, K) contains Fe maps prepared from images below and above the iron edge (700 and 710 eV) – brighter pixels indicate higher iron concentration. The third column (C, F, I, L) contains C maps prepared from images below and above the C edge (280 and 290 eV) – brighter pixels indicate higher carbon concentration. All scale bars are 10 μm except for those for D – F, which are 5 μm.

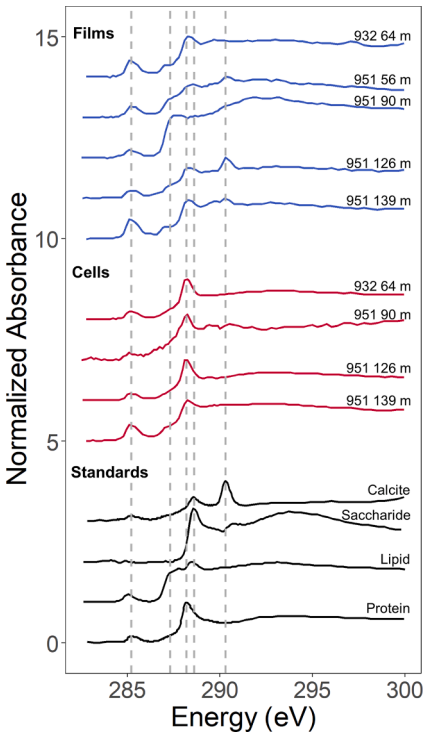

Fig. 6. Representative C X-ray absorption near-edge structure (XANES) spectra from selected films and cells, as well as reference materials of interest. Films had a broad range of spectral features and included properties reminiscent of proteins, saccharides, lipids, and calcite. Cells were more homogenous, containing features reminiscent of proteins. Dashed lines indicate the following energies: 285.2 eV, associated with the 1 s → π* transition in unsaturated or aromatic C, 287.3 eV, associated with the 1 s → σ transition in aliphatic C and in aromatic carbonyl or hydroxyl groups (commonly diagnostic of lipids), 288.2 eV, with the 1 s → π* transition in amide bonds (commonly diagnostic of proteins), 288.6 eV, associated with the 1 s → π* transition in carboxyl and ester groups (commonly diagnostic of polysaccharides), and 290.3 eV associated with the 1 s → π* transition in carbonates (Benzerara et al., 2005; Toner et al., 2009; Chan et al., 2011).

depths of borehole 951 were relatively homogeneous – all had a strong, broad peak at 708.0 ± 0.2 eV and a weaker, broad peak at 720.8 ± 0.1 eV. These spectra are consistent with ferrous iron in sulfide minerals. Some particulate spectra from the 90 and 139 m depths of borehole 951 had additional peaks at 709.6 ± 0.2 and 722.6 ± 0.3 eV. These peaks likely represent ferric iron resulting from particle oxidation during sample loading – when samples from one of these depths were re-prepared and re-analyzed at the STXM, these peaks were not observed. Though it is possible that the peaks at 709.6 eV come from structural Fe(III) in greigite, Fe L-edge XANES spectra for greigite do not consistently have a peak at this energy; peaks around 709.5 eV in greigite spectra are instead commonly attributed to surface oxidation (Zhu et al., 2018).

Fe XANES spectra were also collected from iron associated with carbon within the particulate samples (Fig. 7, film-associated spectra). Based on morphology as observed via STXM, these spectra are consistent with iron adsorbed to biofilms ('Film-associated iron'). Overall, the relative iron concentration in these C-rich phases as determined from iron density maps (Fig. 4, Fig. 5) was lower than the concentrations observed in the minerals. The spectra collected from all five samples for film-associated iron were homogeneous and had a small peak or shoulder at 708.0 ± 0.2 eV, a large, sharp peak at 709.5 ± 0.1 eV, and two weaker peaks at 721.1 ± 0.3 and 722.6 ± 0.2 eV. The spectral peaks from this film-associated iron are consistent with those observed in the ferrihydrite standard, suggesting that this film-associated iron is sorbed Fe(III) (Toner et al., 2009). This sorbed Fe(III) is observed even in samples with no other signs of oxidation – in the borehole environment, aqueous Fe(III) may preferentially sorb to biofilms even at low concentrations of Fe^{3+} (aq). Alternatively, it could be sorbed Fe(II) that is sensitive to oxidation despite careful handling procedures.

3.3. Thin Section Analysis

Rock cores were analyzed for mineralogy and geochemistry to better understand the distribution of primary and alteration minerals along rock fractures and pore spaces that could support microbial life. In the rock core from borehole 932 at a depth of 39 m, a portion of BIF bisected by circular fractures roughly 0.5 cm in diameter was selected for further analysis (Figure S26). The bulk BIF hand sample contained white, red-pink, and dark gray layers. The interior of the fractures had a brown coating not apparent in the bulk hand sample. A thin section was prepared from this region of the core and analyzed via petrographic light microscopy. The BIF was composed of 50–750 mm thick bands of iron-rich and iron-poor rock. In the iron-rich regions, circular iron oxide grains were bound together with infilled quartz cement. The iron-poor regions also contained circular iron oxide grains in a quartz matrix; however, the iron oxide grains in this region were smaller in size and less abundant.

The micron-scale mineralogy and element distributions were analyzed in more detail using electron microprobe analysis (EMPA) and synchrotron-based μ-XRF mapping (Fig. 8) and μ-XRD (Figure S29) to determine the micron scale mineralogy of the BIF. The mineralogy will

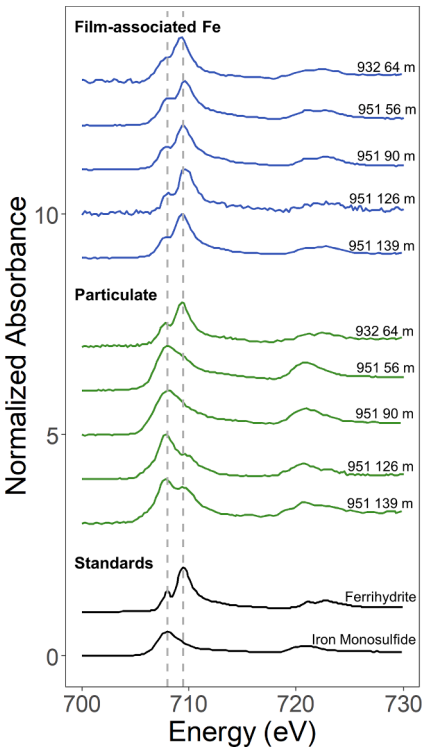

Fig. 7. Representative Fe X-ray absorption near-edge structure (XANES) spectra from biofilm-associated iron, particulate, and reference materials of interest. Both the film-associated iron and the mineral particulate from borehole 932 resembled ferric iron, while the mineral particulate from borehole 951 resembled ferrous iron sulfide. Dashed lines indicate the following energies: 708 eV, associated with Fe(II) in iron sulfides, and 709.5 eV, associated with ferric iron (Toner et al., 2009).

be described here in transect, beginning with the bulk rock (Figure S27) and moving out to the edge of the fracture surface (Figure S28). μ-XRD showed that the iron oxide component of the BIF was entirely hematite. A Ti-bearing mineral was distributed evenly as small grains through both the iron-rich and iron-poor bands and was identified as rutile (TiO_2) via μ-XRD. A Ca-bearing mineral was abundant in the iron-poor bands and present in the iron-rich bands, though at a lower concentration; this phase was identified as fluorapatite ($Ca_5(PO_4)_3F$) using μ-XRD. Finally, a low-abundance iron-magnesium chlorite ($(Fe,Mg)_5Al(Si_3Al)O_{10}(OH)_8$) was mixed into the iron-rich bands; it could be distinguished from the hematite in XRF maps via its high Mn/Fe ratio. Approaching the fracture, the rock was highly enriched in fluorapatite and depleted in hematite. Following this Ca-rich region, the fracture was coated in a layer composed of chlorite and quartz. Outside of the chlorite/quartz layer, needles of an iron rich mineral phase grow into void space. μ-XRF mapping showed that this mineral phase was chemically distinct from hematite due to an enrichment in arsenic. μ-XRD identified the iron-rich mineral in the fracture as goethite (α-FeOOH).

3.4. Microbial Communities

Metagenome-assembled genomes (MAGs) were reconstructed for nine water and particulate samples (Table 2). These included two new water samples each from boreholes 932 and 944, a new water sample from borehole 951, a particulate sample from the 56 m depth from borehole 951, and three legacy water samples that had previously been described (Sheik et al., 2021). Legacy samples were included to expand the time scale on which the boreholes were compared, and samples from borehole 944 were included to provide another point of comparison to boreholes 932 and 951. Sixty-six high-quality MAGs were assembled with a median completeness of 98 % (completeness ranged between 81.1–100 %) and a median contamination of 1.3 % (contamination ranged between 0–15.1 %). The recovered MAGs span eight phyla and show distinct trends in relative abundance in different boreholes (Fig. 9A). The microbial communities in individual boreholes were also compared using NMDS (Fig. 9B). Samples from borehole 951 clustered together regardless of sampling year, and both water and particulate samples from this borehole were found to be statistically distinct from samples from boreholes 932 and 944.

In boreholes 932 and 944, Bacillota (formerly Firmicutes) and Pseudomonadota (formerly Proteobacteria) were the most abundant phyla in all but one timepoint, though their relative abundance varied. In borehole 932, the relative abundance of Bacillota ranged from 23.7 – 42.7 % of the overall microbial community, while the relative abundance Pseudomonadota ranged from 20.0 % – 60.6 %. In borehole 944, the relative abundance of Bacillota ranged from 6.3 – 42.6 % while that of Pseudomonadota ranged from 40.7 – 73.9 %. In the borehole 944 sample from February 2019, Desulfobacteriota (only a minor component of the borehole community in the other borehole 944 samples, with a relative abundance below 1 %) was more abundant than Bacillota with a relative abundance of 31.8 %. In contrast, in samples from borehole 951, Bacillota was abundant, with a relative abundance ranging from 19.7 – 25.9 % while Pseudomonadota was only a minor component of the borehole's microbial community, with a relative abundance between 0.5—1.3 %. Additionally, despite being minor components of boreholes 932 and 944, Desulfobacteriota and the archaeal phylum Halobacteriota were abundant in all samples from borehole 951, with relative abundances ranging from 10.0 – 43.1 % for Desulfobacteriota and 20.2—51.0 % for Halobacteriota. Actinomycetota was consistently observed as a minor component of the microbial community, with relative abundance below 5 % in all samples. Bacteridota was a minor component in all water samples (relative abundance below 1 %) but were slightly more prominent in the mineral particulate community (relative abundance of 1.9 %). Finally, Spirochaetota and the fully uncultured phylum UBP18 were observed as minor components of the microbial community in some samples (relative abundance below 1 %) – though not always detected, they were present in at least one sample from each borehole.

An indicator species analysis was performed to determine which species were preferentially found in samples from a given borehole (Table S5). Many of the taxa identified in this analysis, regardless of the specific borehole, are known to promote sulfur cycling in diverse environments. Four species were found for borehole 932. The indicator species for this borehole are the least well described in published literature and represent taxa that are novel or uncultured at the level of family (two species, one from the order Pseudomonadales and another from the order Halanaerobiales), order (one species, from the class Moorellia), or even phylum (UBP18). Three species were found to be indicators for samples from borehole 944: one was related to aerobic heterotrophs (*Roseovarius sp016278295)* and two to sulfur oxidizers (novel species of the genera *Thiohalophilus* and *Halothiobacillus*) (Labrenz et al., 1999; Kelly and Wood, 2000; Sorokin et al., 2007). Finally, six species were identified as distinctive to the borehole 951 community; their relatives include sulfur reducers (novel species from the genera *Methanolobus* and *Dethiosulfibacter)* and oxidizers (a novel family of the order Peptostreptococcales), iron reducers (a novel genus of the family *Desulfocapsaceae)*, fermentative heterotrophs (a novel genus from the family *Syntrophotaleaceae*), and methanogens (the novel *Methanolobus* described previously) (Takii et al., 2007; Lai, 2019; Baesman et al., 2021; Sheik et al., 2021).

The shotgun-sequenced metagenomes were also analyzed for genes pertaining to important metabolic processes related to C, N, Fe, and S metabolisms. A diverse array of genes related to sulfur reduction and oxidation were found in all samples (Fig. 10). All metagenomes contained complete pathways for the reduction of sulfate to sulfite: sulfate adenylyltransferase (*sat*), adenylylsulfate reductase (*aprAB*), and the full

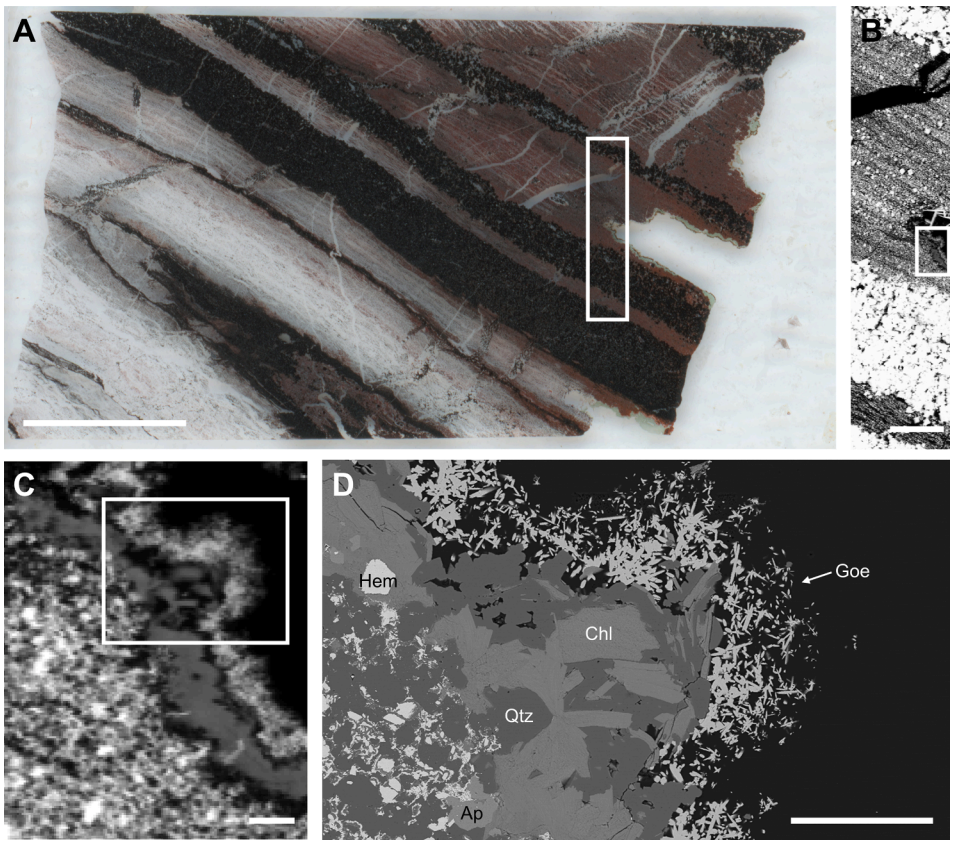

Fig. 8. A. Image of a thin section prepared from a banded iron formation (BIF) region containing a fracture. The white box indicates an area investigated using micro-X-ray fluorescence (μ-XRF) mapping. Scale bar 1 cm. B. μ-XRF map showing iron fluorescence across the area indicated in A. The white box indicates an area investigated at a higher resolution. Scale bar 1 mm. C. μ-XRF map showing iron fluorescence across the area indicated in B. The white box indicates the area imaged via electron microprobe analysis (EMPA). Scale bar 100 μm. D. EMPA image of area indicated in C. Example grains of each mineral observed at the fracture edge are labeled. Scale bar 100 μm.

suite of dissimilatory sulfite reductase (*dsr*) genes. The anaerobic sulfite reductase (*asrABC*) genes associated with sulfite reduction were found in all samples except for the Feb-2019 borehole 944 sample. The sulfur reductase (*Sre*) pathway, used for the reduction of elemental sulfur to sulfide, was not found in any genomes (Laska et al., 2003). Genes associated with sulfur oxidation were found across all samples. Components of the sulfur-oxidizing *Sox* pathway were found in all samples, though *soxB* and *soxC* were missing from the borehole 951 Feb-2019 metagenome and *soxY* was missing from the borehole 951 56 m particulate metagenome. The sulfide:quinone oxidoreductase (*sqr*) pathway was found in all samples. Finally, the thiosulfate/polysulfide reductase chain A (*phsA*) gene, associated with thiosulfate disproportionation, was found in all samples.

The metagenomes for every sample had genes related to carbon fixation via both the Wood-Ljungdahl pathway and the Calvin-Benson-Bassham cycle (identified by the presence of the form II RuBisCO encoding genes). All metagenomes contained the methyl-coenzyme M reductase (*mcrABC*) genes necessary for methanogenesis. The methane/ammonia monooxygenase (*pmoABC*) genes, linked to methane oxidation, were only observed in samples from borehole 932. All metagenomes contained a broad suite of genes related to nitrogen reduction. Additionally, all metagenomes contained the nitrogenase protein (*nifH*, *nifD,* and *nifK*) genes related to N_2 fixation, but no genes related to nitrogen fixation via the alternative nitrogenases *Anf* or *Vnf*. Multiheme cytochromes, often associated with microbial iron reduction, were identified in all metagenomes. One of the metagenomes from borehole 944 also carried homologs to the *extEFG* gene cluster, which was shown to be involved in Fe(III) reduction in *Geobacter sulfurreducens* (Jiménez et al., 2018).

4. Discussion

Boreholes 932 and 951 both contained abundant volumes of mineral particulate. The particulate in borehole 951 accumulated at the bottom of the borehole and in discrete locations throughout the borehole's length. These areas of particulate accumulation were often near fractures, suggesting that the particulate either formed within fractures or precipitated when fracture water entered the borehole, as bioaggregates can readily form in fracture flows (Lee et al., 2023). The borehole 951 particulate was primarily composed of the iron sulfide minerals mackinawite and greigite. The sulfide minerals found in borehole 951 are not seen in the greater host rock and likely formed as a result of biogeochemical iron and sulfur reduction within the borehole or the fracture networks which intersect the borehole. Mackinawite (FeS) and greigite (Fe_3S_4) are not typically primary minerals weathered from rocks, but rather form in anoxic environments as a result of microbial sulfate reduction (Morse et al., 1987; Picard et al., 2018; Jørgensen et al., 2019). The particulate in borehole 932 was composed of hematite and quartz; the differences in mineralogy suggest different particulate sources between the two boreholes. The borehole 932 particulate and the quartz observed in 951 consisted of fine mineral grains, likely from the host rock – both hematite and quartz can be found in the BIF contained within the Soudan formation (Schuler et al., 2022). This particulate was likely introduced during mine operations after the boreholes were drilled, and if sulfide mineral-forming processes are also occurring in borehole 932, they must be occurring below the point at which the quartz-hematite particulate obstructs the borehole. The composition of the mineral particulate, particularly that observed in 951, provides evidence of robust Fe and S biogeochemical cycles in the deep lithospheric

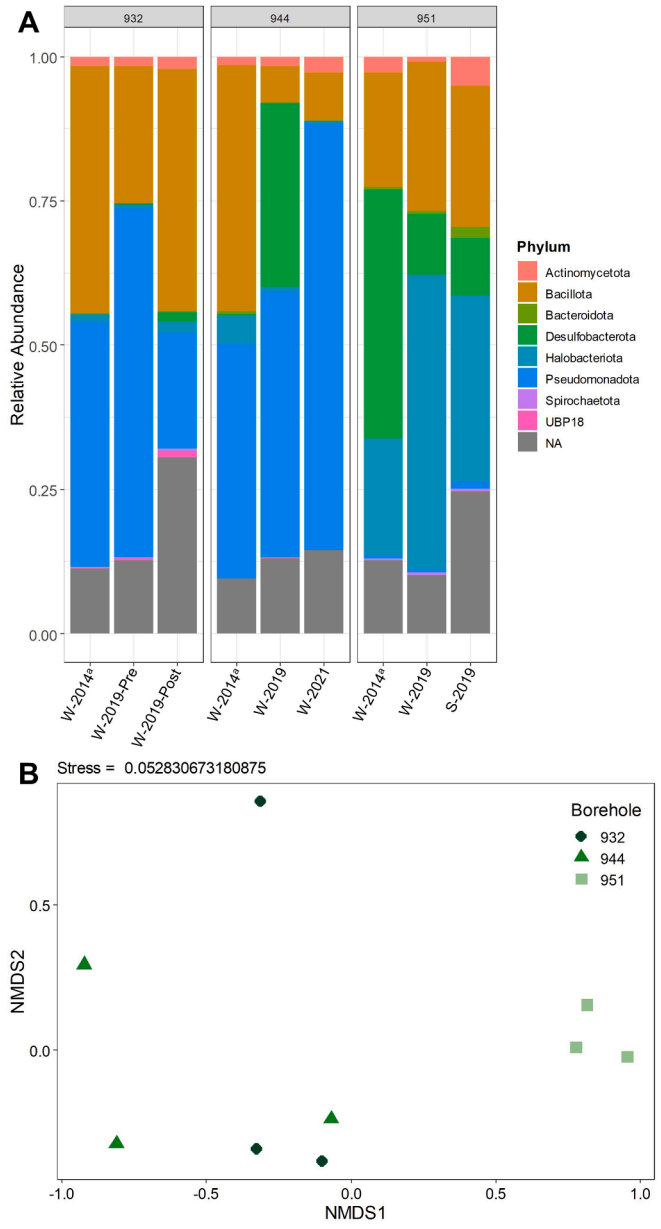

Fig. 9. A. Relative abundance of bacterial and archaeal phyla in assembled metagenomes from water ("W-") and mineral particulate ("P-") samples. All samples were filtered from groundwaters flowing from boreholes except for the particulate from 951 (collected from 56 m into the borehole). "NA" denotes contigs that were not mapped onto any bins and thus lack phylogenetic assignment. [a]Data from these samples were previously published (Sheik et al., 2021). B. Non-metric multi-dimensional scaling (NMDS) plot for the metagenomes. Both the water and particulate samples for borehole 951 are more similar to each other than to the samples from boreholes 932 and 944.

biosphere. The mineral particulate from both boreholes was also associated with both cells and biofilm, providing evidence of robust surface-attached microbial communities and extracellular reserves of organic carbon in the continental subsurface.

4.1. Evidence of Iron and Sulfur Cycling in Fractures

The deep fracture networks accessed by Soudan Mine boreholes likely contain active and linked iron and sulfur cycles driven by both microbial activity and abiotic reactions with iron oxide minerals (Fig. 11). Sulfate has been consistently detected in borehole waters, with concentrations averaging 0.8 ± 0.3 mM (Schuler et al., 2022). Thermodynamic modeling has suggested that sulfate reduction is energetically favorable via electron donors like methane or other short-chain alkanes present in the Soudan borehole fluids (Dowd et al., 2022). Indeed, sulfur-reducing microorganisms are ubiquitous in deep subsurface environments similar to those accessed by the Soudan Mine (Stevens and Mckinley, 1995; Baker et al., 2003). The metagenomes collected from borehole waters and particulate further show the potential for sulfate reduction by the presence of *sat*, *apr*, and reductive *dsr* genes (Fig. 10) that work sequentially to activate and reduce sulfate to sulfide. Although we know that sulfate reduction is likely occurring in the Soudan fractures, no H_2S has been detected in either the waters or their associated gases. Evidence for sulfate reduction instead comes from the active formation of mackinawite and greigite. The high iron concentrations in the Soudan waters, averaging 1.7 ± 0.4 mM, likely induce the precipitation of mackinawite, keeping total dissolved sulfide (ΣH_2S) concentrations below detectable levels (Schuler et al., 2022). Additionally, the BIF at Soudan contains large quantities of hematite, and this may also be partially responsible for the low total sulfide concentrations at Soudan. Hematite can oxidize aqueous H_2S and form intermediate sulfur species (S_{int}) like elemental sulfur (S_0) and thiosulfate ($S_2O_3^{2-}$) (Pyzik and Sommer, 1981; Poulton et al., 2004). The oxidation of ΣH_2S by hematite will also cause the reductive dissolution of iron, leading to the release of Fe^{2+} (aq) to Soudan waters. Iron reduction is also likely facilitated microbially as indicated by the abundance of multiheme cytochromes and the *extEFG* gene cluster found in the Soudan metagenomes. Prior work at Soudan has also predicted genes associated with Fe(III) reduction, and a ferric iron reducing bacterium, *Desulfuromonas soudanensis WTL*, has been isolated from Soudan groundwaters (Badalamenti et al., 2016; Sheik et al., 2021). Mackinawite, once formed through microbial sulfate and Fe(III) reduction, will transform into greigite in the presence of an oxidant. Though the Soudan waters are anoxic, polysulfides can also catalyze this reaction (Schoonen and Barnes, 1991b; Hunger and Benning, 2007; Dowd et al., 2022). Elemental sulfur, generated by the reactions between hematite and ΣH_2S, can react with sulfide to form polysulfides (S_n^{2-}). Thus, the presence of greigite is further evidence of an oxidant-driven branch of the sulfur cycle, with Fe(III)-bearing hematite likely being the most abundant oxidant in the Soudan fracture network.

Iron sulfide minerals are ubiquitous in chemically reducing sedimentary environments and commonly include mackinawite, greigite, and pyrite (FeS_2); however, the specific sulfides formed depend on the geochemical and microbial conditions of a given location (Morse et al., 1987; Rickard and Luther, 2007; Picard et al., 2018). These minerals generally form due to the metabolic activity of dissimilatory iron- and sulfur-reducing bacteria – the reduction of Fe(III) and SO_4^{2-} (aq) results in increased concentrations of Fe^{2+} (aq) and ΣH_2S (g, aq), causing the precipitation of iron sulfides (Rickard, 1969; Herbert et al., 1998; Williams et al., 2005). Iron sulfide precipitates have been observed in several deep subsurface environments, co-occurring with sulfate and metal-reducing microorganisms (Olson et al., 1981; Baker et al., 2003). The formation of iron sulfide minerals has been suggested as the cause of low observed ΣH_2S concentrations at several deep crustal research sites, including the Soudan Mine (Li et al., 2016).

Mackinawite and greigite often occur as metastable precursor phases to pyrite (Schoonen and Barnes, 1991b). Though the formation of pyrite is thermodynamically favorable in environments with elevated ferrous iron and ΣH_2S concentrations, pyrite precipitation occurs slowly at temperatures below 100 °C (Schoonen and Barnes, 1991a). Conversely, mackinawite precipitation can occur quickly; in many reducing environments, iron and ΣH_2S concentrations are in equilibrium with mackinawite precipitation rather than the more stable but slower-forming sulfide phases (Schoonen and Barnes, 1991a). Mackinawite can further react with polysulfides, forming greigite, which can react with either hydrogen sulfide species or polysulfides to form pyrite (Schoonen and Barnes, 1991b; Hunger and Benning, 2007; Rickard and Luther, 2007). Even at temperatures as low as 10 °C, mackinawite is expected to be

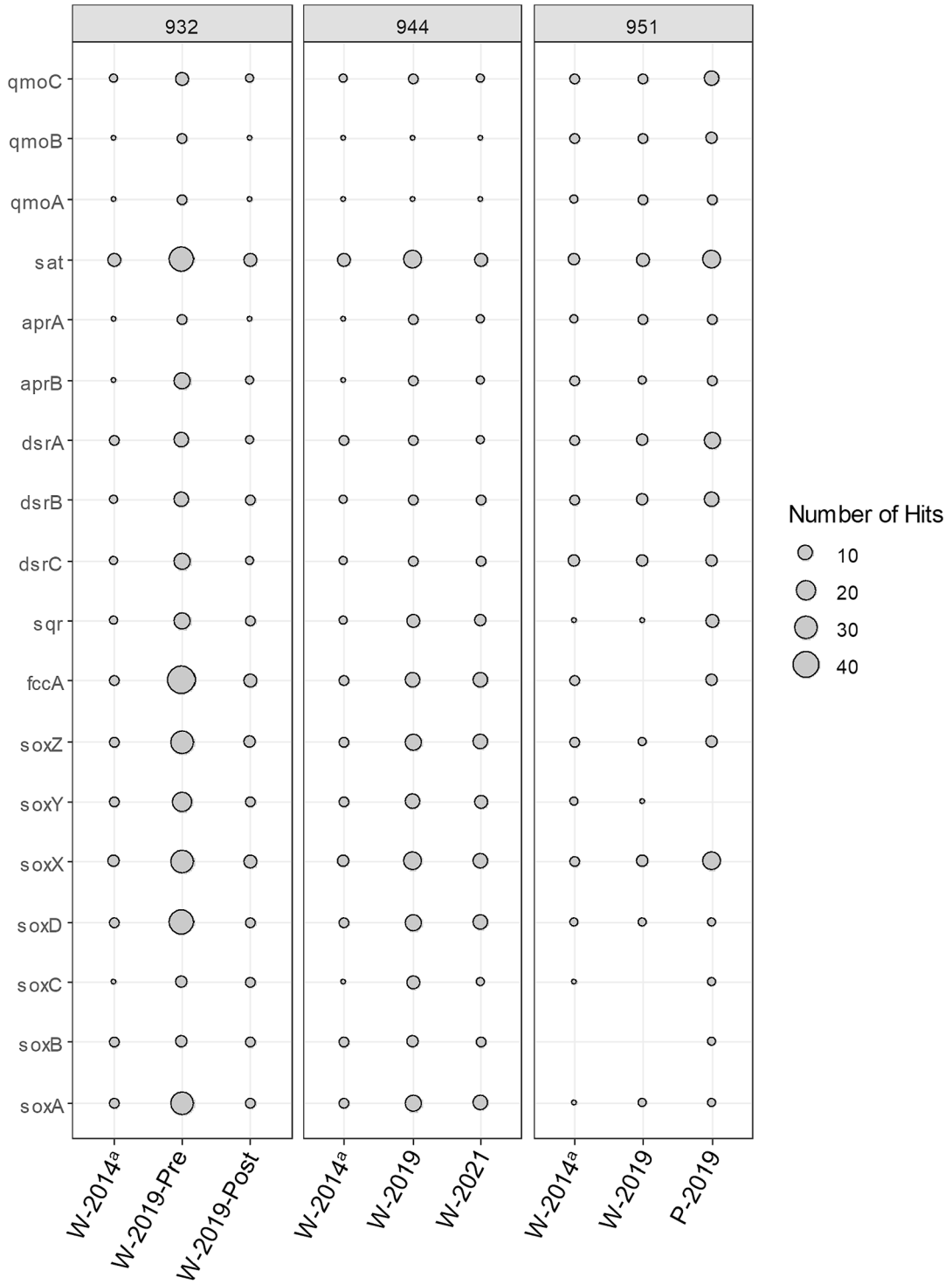

Fig. 10. Microbial sulfur metabolisms present in the metagenomes. Sample names beginning with a "W" indicate water samples, while the sample name beginning with "P" indicates a particulate sample. The numbers in the sample names indicate the year in which the sample was collected. [a]Data from these samples were previously published (Sheik et al., 2021).

fully converted to pyrite over a timeframe of several weeks with sufficient sulfur flux (Hunger and Benning, 2007). The absence of secondary pyrite in the Soudan fracture network shows that, despite the presence of primary pyrite in the host rock, there is not enough ΣH_2S in the water to convert mackinawite and greigite to pyrite.

In addition to forming Fe sulfide minerals, ΣH_2S could be consumed through reactions with the abundance of iron oxide minerals at Soudan, which may oxidize sulfide before it is able to react with mackinawite or greigite (Pyzik and Sommer, 1981; Elsgaard and Jørgensen, 1992; Poulton et al., 2004; Zhang et al., 2016). This reaction could contribute to a cryptic sulfur cycle: sulfate is continually resupplied and thus maintains a relatively consistent concentration, while other sulfur phases are short-lived and difficult to detect. Mackinawite seems to be more prominent in the deeper samples, collected from the portion of the borehole rich in hematite ore and BIF, while greigite is largely found in the upper samples, collected from chlorite schist. The iron oxides likely

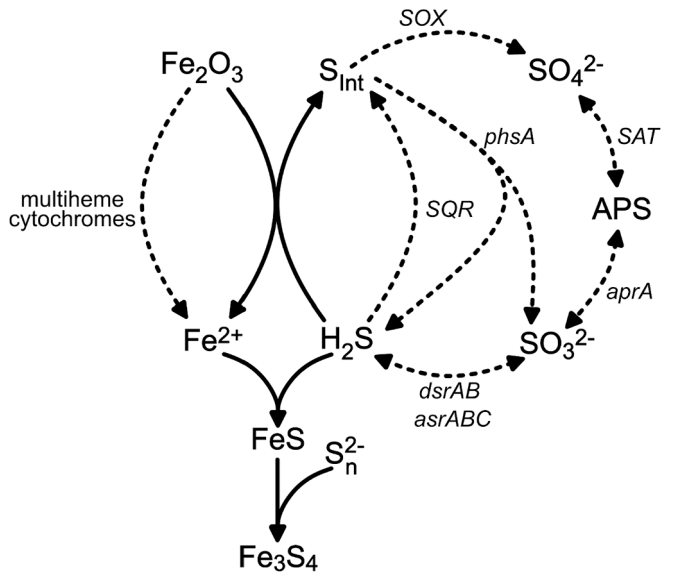

Fig. 11. Diagram of the proposed linked iron and sulfur cycles in the Soudan fracture network. Solid arrows indicate proposed abiotic reactions, while dashed lines indicate reactions that may be facilitated by microorganisms. These arrows are labeled with the corresponding genes detected in the metagenomes from Soudan waters and particulate. S_{Int} is used as a stand-in for several possible intermediate-valence sulfur species, namely elemental sulfur and thiosulfate.

scavenge ΣH_2S, forming the sulfur intermediates elemental sulfur and thiosulfate (Pyzik and Sommer, 1981; Elsgaard and Jørgensen, 1992; Poulton et al., 2004). These reactions may be drawing total sulfur concentrations below those required for greigite formation. Intermediate sulfur compounds could then be microbially reduced back to hydrogen sulfide (which can re-react with hematite) and oxidized to sulfate through a sulfite intermediate. The *phsA* pathway, which disproportionates thiosulfate in this manner, was detected in all metagenomes (Fig. 10). The *Sox* pathway, which can also oxidize these sulfur intermediates to sulfate, was found in many of the metagenomes. In fractures where there is sufficient ΣH_2S, hydrogen sulfide may instead react with elemental sulfur to form polysulfides. These dissolved polysulfide species can react with mackinawite, forming greigite. This acts as a sink for both hydrogen sulfide and for the polysulfides, ending further biogeochemical redox cycling of sulfur. Overall, the particulate and waters provide both chemical and microbiological evidence for iron and sulfur reduction as well as robust and linked Fe and S cycles.

The iron sulfide minerals in borehole 951 reflect either the geochemical and microbial conditions of the surrounding fractures or the borehole itself. These conditions could differ, either due to disturbance of the system during drilling or due to the mixing of water from multiple active fractures within the borehole, combining sources with potentially contrasting chemical properties. The boreholes have had six decades of continuous positive-pressure flow of groundwater, so the initial drilling disturbance has been diminished compared to newly drilled boreholes. Additionally, the mixing of fracture waters with different chemistries is expected to occur naturally and can create niches in the subsurface with abundant energy sources for microbial life (Bochet et al., 2020). Current borehole conditions can be used along with rock cores to interpret plausible *in situ* fracture conditions. In particular, alteration minerals in fractures from original rock cores can record chemical weathering and secondary mineral formation processes.

Minerals observed in fractures in Soudan rock cores are consistent with *in situ* formation of FeS, suggesting that sulfide formation occurs in the fracture network as well as in the borehole and that these mineral-forming processes were active before any drilling or disturbance of the Soudan fracture network. Acicular goethite crystals were observed along fracture surfaces from the BIF (Fig. 8). Goethite is not observed in the bulk rock of the BIF, making it distinct from the iron oxides in the surrounding rock formation. Iron oxides are unlikely to form *in situ* in heavily reducing environments such as those in Soudan. Although Soudan has a high concentration of iron in its groundwaters (Schuler et al., 2022), this is likely to be almost entirely Fe^{2+}, which has a much higher solubility than Fe^{3+} at circumneutral pH. An oxidant such as O_2, NO_3^-, or Mn(IV) would be required to oxidize Fe^{2+} (aq) and form goethite, yet none of these are observed within the Soudan formation or associated groundwaters. Alternatively, the goethite could have precipitated after the drilling of the core; however, the concentration of iron in the Soudan groundwater is prohibitively low for a goethite rind as thick as the one observed to precipitate during the drying of wet core (***S5.2 Goethite Rind Precipitation***). The most probable explanation for the observed goethite rind is the oxidation of an authigenic iron sulfide rind after drilling, and the existence of such a rind would imply that the processes described above were active in the Soudan fracture network before any drilling took place. Studies have shown that goethite can form as a result of both the dry and wet oxidation of mackinawite (Boursiquol et al., 2001; Jeong et al., 2010). Iron oxyhydroxides are commonly observed alteration minerals on fracture surfaces, even among those drilled from presumably reducing aquifers (Kloppmann et al., 2002). This suggests that the oxidation of iron-sulfide rinds is a common occurrence on fracture surfaces from recovered rock cores. The probable ubiquity of this process points to the relevance Fe and S cycling in the Soudan Mine to other deep continental systems. The mineral and aqueous phases identified here can serve as markers for similar processes occurring elsewhere in the crust, shedding light on the mechanisms through which biogeochemical cycling supports crustal life.

4.2. Cells and Biofilm Associated with Mineral Precipitate Aggregates

Carbonaceous particles resembling a number of different microbial cell morphologies, including rods, filaments, cocci, and spores, were observed in every mineral precipitate sample. Morphologies resembling the tufted or filamentous fabrics characteristic of EPS or biofilm were also observed in all samples, primarily in association with minerals. Though cells and biofilms were observed in all samples, they were not evenly distributed. In borehole 951, where mineral precipitates were characterized along a depth profile, both cells and biofilms increased in abundance with depth. Both the deepest samples from this borehole and the sample from borehole 932 showed evidence of a robust biofilm-hosted community. Microbial communities in the curst are not just composed of chemolithoautotrophs but also include heterotrophic organisms sustained by autotrophic primary production (Onstott et al., 2006; Hubalek et al., 2016; Sheik et al., 2021). The abundance and activity of these heterotrophic organisms are controlled by the form and availability of organic carbon (Hubalek et al., 2016; Magnabosco et al., 2018b). Characterizing the abundance and nature of organic materials in the subsurface provides important information about the microbial ecology and activity of the deep biosphere.

The cells and biofilms in these samples had chemically distinct organic C speciation. Cells had spectral features consistent with unsaturated carbon species and carboxylic acids and resembled reference spectra for proteins and microbial cells from natural samples (Lehmann et al., 2009; Toner et al., 2009; Chan et al., 2011). Previous STXM studies of cells in both lab-grown and environmental samples have found that whole-cell spectra commonly resemble protein standards due to the abundance of peptides and other carboxylic-acid-bearing biomolecules in their cell walls and membranes (Brandes et al., 2004; Chan et al., 2011). The spectra for the films were more heterogeneous and likely reflect the presence of multiple biological polymers in the biofilm material, such as proteins and saccharides. This is consistent with previous C XANES studies of biofilms (Lawrence et al., 2003). Spectral analysis suggests a change in composition with depth –saccharides were observed uniformly, while protein and lipid abundance increased with

depth. Biofilms were less abundant in the shallower samples, and cells and films were never observed within the same STXM image in the shallowest two samples. While the films in these shallower samples are likely microbially derived, these observations indicate overall greater biofilm-hosted microbial biomass in the deeper samples.

There are several possible explanations for the increase in microbial biomass and biofilm with depth. The deepest samples in the borehole may also contain the oldest particulate – larger FeS particles likely settled to the bottom of the borehole, meaning that the mineral particulate samples from the deepest regions may have been residing within the borehole for years or decades. Thus, the increased biomass on the deepest mineral aggregates could result from increased time for microorganisms to colonize those mineral aggregates. However, the deeper mineral particulate samples are hosted within the BIF and the hematite ore body, allowing for cryptic sulfur cycling and microbial Fe(III) reduction not possible in the shallower schist-bearing region. The increase in microbial biomass in the deeper samples could be due to the energy available to microorganisms through Fe(III) reduction and the reduction and oxidation of sulfur intermediates in the fractures intersecting the borehole at this depth. This theory is supported by the cell density observed via SEM and STXM on the comparatively shallow hematite-quartz sediment from borehole 932. Ultimately, both mechanisms could be working in tandem to drive cell density on these deeper samples.

Biofilms are directly tied to many of the most pressing questions related to the deep biosphere today. Biofilm and surface-attached cells are expected to outnumber planktonic cells in the subsurface by a factor of 100 or more (Hazen et al., 1991; Lehman et al., 2001; Flemming and Wuertz, 2019). However, there is still some uncertainty with regard to the magnitude of this difference (McMahon and Parnell, 2014; Magnabosco et al., 2018a). Because of this, it is difficult to accurately estimate the overall cell abundance and biomass present in the subsurface and determine whether surface-associated microbes consist of a few attached cells on a rock surface or whether they could potentially be a part of more robust, denser communities. Laboratory incubations of groundwaters from deep fractured-rock have shown that microbes will readily attach and grow biofilms and that surface-attached and biofilm-forming organisms differ from those that dominate free-flowing waters (Lehman et al., 2001; Jones and Bennett, 2017). Biofilms with microbial communities taxonomically distinct from planktonic populations have been grown on glass slides, mineral chips, and polished minerals incubated *in situ* within deep biosphere environments (Pedersen et al., 1996; Ramírez et al., 2019; Casar et al., 2020; Nuppunen-Puputti et al., 2022). Biofilms have also been sampled from boreholes drilled into the subsurface, though these have largely been limited to microoxic locations or those near borehole entrances (MacLean et al., 2007; Borgonie et al., 2015). However, a study combining drilling with careful contamination control was able to characterize microbial communities on fracture surfaces (Jagevall et al., 2011). And a recent drilling study in the Iberian Pyrite Belt found chemical evidence of cells and EPS on fracture surfaces at every depth investigated (Escudero et al., 2018). Our findings contribute to the building evidence that biofilms are a more important aspect of microbial life in the deep continental biosphere than planktonic cells.

Mineral particulate samples such as those collected at the Soudan Mine can expand our understanding of biofilm-hosted life in the deep biosphere. The biofilms hosted on these mineral aggregates are distinctive due to the confluence of their cell-density and the depth at which they were collected. Because most cells within the deep biosphere are likely found within biofilms and the microbial communities in these biofilms differ from planktonic microbial communities, exploring these differences further should be a priority for subsurface research. Incubating mineral chips in deep groundwaters can be an important source of information, but it is important to confirm these experimental results by sampling natural biofilms collected deeper into the subsurface environment. Mineral aggregates incorporating biomass, like those seen at Soudan, could readily emerge in other subsurface fracture networks (Lee et al., 2023). Biomass-mineral aggregates will be easier to sample than rock fracture surfaces – no new drilling will be required for their collection. Consequently, fragile biomaterials will not be destroyed by heat and friction, and contamination will not be introduced through drilling mud or water. Future work in subsurface environments should treat borehole-hosted particulate as a potential repository of subsurface life and thus should prioritize collecting and analyzing particulate carried in borehole effluent and sediments collecting on borehole walls. Studying the surface-attached communities collected on these particles and the chemistry of the particles themselves will provide valuable information about the biogeochemical functioning of crustal environments.

4.3. Microbial Communities in the Soudan Boreholes

The microbial communities in all three boreholes were relatively stable from timepoint to timepoint over five to seven years of sampling. Metagenomes were most similar between boreholes 932 and 944; these two boreholes access the most saline and isolated groundwaters in Soudan, with TDS concentrations between 97,000 – 116,000 mg/L (Schuler et al., 2022). Metagenomes from borehole 951 diverged from those from both 932 and 944. These differences are likely driven by the differences in salinity between the boreholes and by differences in the lithologies accessed by the fractures directing water into the boreholes. Unexpectedly, the metagenomes from the borehole 951 filtered groundwater and 56 m particulate did not differ substantially from one another. However, it should be noted that the particulate sample had fewer cells and EPS (by X-ray and electron microscopy) than those samples from deeper into the borehole. It is possible that the deeper samples with more abundant biofilm communities would have larger, significant differences from the planktonic microbial community. Among the microbial phyla observed, Desulfobacterota underwent the largest fluctuations in relative abundance. This may be connected to the fluctuations in sulfate concentrations observed in the Soudan groundwaters (Schuler et al., 2022). This phylum is linked to sulfate reduction, and its abundance may rise with the availability of sulfate, or temporary spikes in the abundance of this phylum may cause decreases in observed sulfate as the compound is reduced (Langwig et al., 2022).

Indicator species analysis can be used to investigate the biogeochemical differences between otherwise similar borehole environments and microbial communities. The indicator species for borehole 932 are the least similar to microbes which have previously been described in published literature. This borehole is also the most saline and therefore is assumed to access the most isolated groundwater in Soudan. These extreme conditions correlate with uncultivated or understudied microbial phylogenies. Indicator species for borehole 944 contain likely aerobic heterotrophs, including a species from the genus *Roseovarius*. This would seem to indicate that borehole 944 accesses more aerobic fracture conditions than the other two boreholes. However, oxygen concentrations in gas samples are quite low in this and other boreholes and have been attributed to oxygen contamination during sampling rather than to oxic or suboxic conditions within the borehole at depth (Dowd et al., 2022). Borehole 944 has a lower groundwater flow rate than 932 and 951, and it is possible that this allows surficial oxygen to infiltrate deeper into the borehole than it can in the other two boreholes (Dowd et al., 2022). The presence of aerobic heterotroph indicator species may be a sign that a deeper sample is needed to get an uncontaminated representation of the subsurface community in borehole 944. Finally, indicator species for borehole 951 suggest that the microbes in this borehole have the potential to carry out a broad suite of metabolism linked to life in isolated subsurface environments. The borehole contains putative methanogens and fermenters, necessary to drive the carbon cycle that supports life in the subsurface. Microbes in this borehole are also linked to the oxidation and reduction of a broad array of S compounds of varying valence states, providing genomic evidence for a

cryptic sulfur cycle. This cycle could be coupled to Fe or N cycling, as microbes that promote Fe and N cycling are present in this borehole. Overall, the indicator species for borehole 951 resemble the microorganisms found in many remote crustal sites supported by lithotrophs and anaerobic heterotrophs (Wu et al., 2016; Momper et al., 2017a).

Examining MAGs as taxa from these boreholes can provide some information about the possible microbial metabolisms supported in the Soudan fracture networks, but directly examining the genes present in metagenomes gives insight into the metabolic capabilities of the entire community. A focus on the whole microbial community is of particular importance due to the prevalence of metabolic handoffs between species in the deep biosphere (Anantharaman et al., 2016). The genes observed across all samples supported the common theory of the deep biosphere as an environment based on a chemolithoautotrophic metabolic backbone. A broad array of sulfate and sulfite reduction genes were found in the Soudan metagenomes. However, it is important to note that some genes associated with these sulfur pathways can function in both oxidizing and reducing directions and that the presence of these genes is not direct evidence of either sulfur oxidation or reduction (Meyer and Kuever, 2007; Thorup et al., 2017; Kjeldsen et al., 2019). Sulfate reduction to sulfide is an important component in the biogenic formation of iron sulfide minerals in many sedimentary environments. Sulfate reduction capabilities have also been observed in previous genomic studies of Soudan (Sheik et al., 2021). The presence of reduction pathways specific to sulfite, e.g. *Asr*, suggests that this sulfur intermediate may play an important metabolic role in Soudan groundwater communities. The lack of the *Sre* pathway, used in the reduction of elemental sulfur, is interesting in light of the likely formation of S_0 through the reaction of ΣH_2S with hematite. It is possible that elemental sulfur is only oxidized through the *Sox* pathway and not microbially reduced. Alternatively, elemental sulfur precipitates forming at hematite surfaces may only be used by biofilm-hosted microbes, while the planktonic community sequenced in these samples may not have the same access to these compounds.

Genes associated with the oxidation of sulfur species, the *sqr* and *Sox* pathways, were observed in all samples. These genes indicate that thiosulfate oxidation and disproportionation may be important energy-generating metabolisms at Soudan. Like elemental sulfur, thiosulfate is likely to be a product of the oxidation of ΣH_2S by iron oxides (Pyzik and Sommer, 1981; Zopfi et al., 2007). This compound is more soluble than elemental sulfur and thus likely to be more available to planktonic microbes. While reducing environments are generally associated with sulfate reduction, it is increasingly evident that in low-energy environments like Soudan many competing metabolisms may be active at once (Sivan et al., 2014; Treude et al., 2014; Pellerin et al., 2018). Overall, the Soudan microbial communities are well poised to both oxidize and reduce a wide variety of sulfur compounds, providing more evidence that Soudan has a sulfur cycle more complicated than the reduction of sulfate to ΣH_2S, which is then sequestered in iron sulfide minerals. There is likely a diverse and active S cycle in the Soudan fractures, with both S oxidizers and reducers participating depending on local geochemical conditions. The microbial oxidation of elemental sulfur and thiosulfate to sulfate or sulfite could be important parts of a closed sulfur cycle, ensuring that reduced sulfate is regenerated and resupplied to sulfate reducing microorganisms. This regeneration in turn would ensure that sufficient energy is available to support crustal ecosystems for long time scales, preventing any one substrate from being drawn down below metabolically useful concentrations. Because iron oxide minerals also play an essential role in this process, this study also demonstrates the degree to which microorganisms in the deep biosphere depend on rock that makes up their surrounding environment.

5. Conclusion

Geochemical and microbiological investigations at the Soudan Underground Mine revealed mineral-hosted biofilms densely populated by microbial cells as well as a cryptic sulfur cycle coupled to iron cycling. Boreholes drilled into the Soudan formation, a 2.7 Ga BIF located in the southern Canadian Shield, were lined with fine-grained mineral particulate colonized by microbial communities. Mineral surfaces were covered in thick biofilms composed of proteins and polysaccharides and diverse cell morphotypes. The mineralogy and provenance of the mineral particulate differed between boreholes, as one contained quartz and hematite likely introduced to the borehole by mining or weathering while another contained iron sulfide minerals that likely precipitated authigenically. The mineralogy of the iron sulfides differed based on both depth and local rock lithology. Mackinawite was more prominent in deeper hematite-rich regions and greigite in shallower hematite-poor regions. Mineralogical analysis of cores from Soudan suggests that iron sulfide mineral formation likely takes place within fracture networks, not just in the borehole. Sulfide mineral formation was an active process before any drilling or disturbance of the Soudan groundwaters took place and results from microbially mediated Fe(III) and sulfate reduction. Metagenomes assembled from DNA extracted from both the iron sulfide particulate and from the Soudan groundwaters confirm that these crustal microbial communities have the genomic potential to utilize a wide variety of S species, promoting both S reduction and oxidation processes in this anoxic environment. Mineralogical analysis and MAGs together provide evidence for a cryptic sulfur cycle linked to iron cycling that generates sulfur intermediates like elemental sulfur and thiosulfate which could fuel the robust microbial communities colonizing the mineral particulate. Taken as a whole, the geochemical and metagenomic elements of this study suggest that the Soudan fractures contain distinct biogeochemical iron and sulfur cycles linked to microbial populations and fracture-specific mineralogy and fluid chemistry. Overall, this study demonstrates the importance of sulfur as an essential substrate for the deep biosphere and points to fracture-hosted mineral particulate as a key to understanding biofilm-hosted subsurface communities. Future work focused on S XANES, S isotopes, or the quantification of intermediate sulfur species in groundwater will further elucidate how sulfur is cycled in crustal environments and shed more light on the biogeochemical mechanisms supporting deep, isolated microbial communities.

Data availability

XANES spectra, XRD patterns, and the results of metagenome processing are available through the Environmental Data Initiative at https://doi.org/10.6073/pasta/6933c6fa8327eb7be3bd477d2ce978fd. Down-borehole video and XRF maps are available through Figshare at https://doi.org/10.6084/m9.figshare.23865951.v1. Genomic data is available through the National Center for Biotechnology Information (NCBI) Sequence Read Archive (SRA) under BioProject PRJNA248749; specific samples can be found under sequence numbers SRR24974068, SRR24974071, SRR24974070, SRR24974065, SRR24974067, and SRR24974066.

CRediT authorship contribution statement

Christopher J. Schuler: Formal analysis, Investigation, Writing – original draft, Writing – review & editing, Conceptualization, Methodology. **Amanda Patsis:** Formal analysis, Investigation. **Scott C. Alexander:** Conceptualization, Investigation. **David Hsu:** Investigation. **William S. Dowd:** Investigation. **Woonghee Lee:** Investigation. **Sarick L. Matzen:** Investigation. **Matthew A. Marcus:** Investigation. **Cody S. Sheik:** Conceptualization, Funding acquisition, Supervision. **Jill M. McDermott:** Conceptualization, Funding acquisition, Supervision. **Peter K. Kang:** Conceptualization, Funding acquisition, Supervision. **Cara M. Santelli:** Conceptualization, Funding acquisition, Supervision, Investigation, Writing – review & editing. **Brandy M. Toner:** Conceptualization, Funding acquisition, Supervision, Investigation, Writing – review & editing.

Declaration of competing interest

The authors declare that they have no known competing financial interests or personal relationships that could have appeared to influence the work reported in this paper.

Acknowledgements

We thank the Minnesota Department of Natural Resources for allowing us to access the Soudan Underground Mine State Park. We are especially grateful to James Essig, Park Manager at Soudan, and his staff – without their time and guidance, this research would not have been possible. This research was supported by funding from the NSF Integrated Earth Systems Program (Award Number EAR-1813526). Parts of this work were carried out at the Characterization Facility, University of Minnesota, which receives partial support from the NSF MRSEC (Award Number SMR-2011401) and the NNCI (Award Number ECCS-2025124). This research used resources from the Advanced Light Source, which is a DOE Office of Science User Facility under contract no. DE-AC02-05CH11231. This research used resources of the National Synchrotron Light Source II, a U.S. Department of Energy (DOE) Office of Science User Facility operated for the DOE Office of Science by Brookhaven National Laboratory under Contract No. DE-SC0012704. The allocated beamtime at 4-BM was also supported by a partner user agreement funded by the NSF (Award Number EAR-1634415).

We thank Seema Thakral and Javier Garcia Barriocanal for powder XRD data collection. We thank Anette von der Handt for guidance during electron microprobe analysis. We thank Nicholas Seaton for their help with electron microscopy. We thank Sarah Nicholas, Ryan Tappero, Brandy Stewart, and Rose Jones for assistance in data collection at the NSLS-II. We thank Daniel Bond for his helpful feedback during manuscript preparation.

Appendix A. Supplementary material

The supplementary material included along with this paper contains additional field observations, geochemical measurements, and analyses of the metagenomes. The document specifically includes information on down-borehole video of boreholes 932 and 951, XRD patterns for all mineral particulate samples, additional SEM and STXM imaging of the particulate samples, all C and Fe XANES spectra of the particulate and associated biomaterials, XRF mapping and μ-XRD characterizing a thin section prepared from the Soudan BIF, calculations investigating the feasibility of goethite precipitation on core samples, statistical information on the metagenome samples, and the full results of indicator species analyses for boreholes 932, 944, and 951.

Supplementary material to this article can be found online at https://doi.org/10.1016/j.gca.2024.04.019.

References

Alneberg, J., Bjarnason, B.S., De Bruijn, I., Schirmer, M., Quick, J., Ijaz, U.Z., Lahti, L., Loman, N.J., Andersson, A.F., Quince, C., 2014. Binning metagenomic contigs by coverage and composition. Nat. Methods 11, 1144–1146.

Anantharaman, K., Brown, C.T., Hug, L.A., Sharon, I., Castelle, C.J., Probst, A.J., Thomas, B.C., Singh, A., Wilkins, M.J., Karaoz, U., Brodie, E.L., Williams, K.H., Hubbard, S.S., Banfield, J.F., 2016. Thousands of microbial genomes shed light on interconnected biogeochemical processes in an aquifer system. Nat. Commun. 7, 13219.

Badalamenti, J.P., Summers, Z.M., Chan, C.H., Gralnick, J.A., Bond, D.R., 2016. Isolation and genomic characterization of "Desulfuromonas soudanensis WTL", a metal- and electrode-respiring bacterium from anoxic deep subsurface brine. Front. Microbiol. 7, 1–11.

Baesman, S.M., Sutton, J.M., Fierst, J.L., Akob, D.M., Oremland, R.S., 2021. Syntrophotalea acetylenivorans sp. Nov., a diazotrophic, acetylenotrophic anaerobe isolated from intertidal sediments. Int. J. Syst. Evol. Microbiol. 71.

Baker, B.J., Wimpee, C.F., Moser, D.P., Onstott, T.C., MacGregor, B.J., Fishbain, S., Jackson, B., Stahl, D.A., Wagner, M., Fry, N.K., Speolstra, N., Loos, S., Takai, K., Fredrickson, J., Lollar, B.S., Balkwill, D., 2003. Related assemblages of sulphate-reducing bacteria associated with ultradeep gold mines of South Africa and deep basalt aquifers of Washington State. Environ. Microbiol. 5, 267–277.

Bakkila (1960a) *Exploration Drill Hole Record: DDH 944*., Virginia, MN.

Bakkila (1960b) *Exploration Drill Hole Record: DDH 951*., Eveleth, MN.

Bell, E., Lamminmäki, T., Alneberg, J., Andersson, A.F., Qian, C., Xiong, W., Hettich, R. L., Frutschi, M., Bernier-Latmani, R., 2020. Active sulfur cycling in the terrestrial deep subsurface. ISME J. 14, 1260–1272.

Benzerara, K., Yoon, T.H., Menguy, N., Tyliszczak, T., Brown, G.E., 2005. Nanoscale environments associated with bioweathering of a Mg-Fe-pyroxene. Proc. Natl. Acad. Sci. 102, 979–982.

Bochet, O., Bethencourt, L., Dufresne, A., Farasin, J., Pédrot, M., Labasque, T., Chatton, E., Lavenant, N., Petton, C., Abbott, B.W., Aquilina, L., Le Borgne, T., 2020. Iron-oxidizer hotspots formed by intermittent oxic–anoxic fluid mixing in fractured rocks. Nat. Geosci. 13, 149–155.

Borgonie, G., Linage-Alvarez, B., Ojo, A.O., Mundle, S.O.C., Freese, L.B., Van Rooyen, C., Kuloyo, O., Albertyn, J., Pohl, C., Cason, E.D., Vermeulen, J., Pienaar, C., Litthauer, D., Van Niekerk, H., Van Eeden, J., Lollar, B.S., Onstott, T.C., Van Heerden, E., 2015. Eukaryotic opportunists dominate the deep-subsurface biosphere in South Africa. Nat. Commun. 6, 1–12.

Boursiquol, S., Mullet, M., Abdelmoula, M., Génin, J.M., Ehrhardt, J.J., 2001. The dry oxidation of tetragonal FeS1-x mackinawite. Phys. Chem. Miner. 28, 600–611.

Brandes, J.A., Lee, C., Wakeham, S., Peterson, M., Jacobsen, C., Wirick, S., Cody, G., 2004. Examining marine particulate organic matter at sub-micron scales using scanning transmission X-ray microscopy and carbon X-ray absorption near edge structure spectroscopy. Mar. Chem. 92, 107–121.

Brandes, J.A., Wirick, S., Jacobsen, C., 2010. Carbon K-edge spectra of carbonate minerals. J. Synchrotron Radiat. 17, 676–682.

Butler, E.C., Hayes, K.F., 1998. Effects of solution composition and PH on the reductive dechlorination of hexachloroethane by iron sulfide. Environ. Sci. Technol. 37, 113–115.

Canfield, D.E., Stewart, F.J., Thamdrup, B., De Brabandere, L., Dalsgaard, T., Delong, E. F., Revsbech, N.P., Ulloa, O., 2010. A cryptic sulfur cycle in oxygen-minimum-zone waters off the Chilean coast. Science 80-.). 330, 1375–1378.

Casar, C.P., Kruger, B.R., Flynn, T.M., Masterson, A.L., Momper, L.M., Osburn, M.R., 2020. Mineral-hosted biofilm communities in the continental deep subsurface, Deep Mine Microbial Observatory, SD, USA. Geobiology 508–522.

Casar, C.P., Momper, L.M., Kruger, B.R., Osburn, M.R., 2021. Iron-fueled life in the continental subsurface: Deep Mine Microbial Observatory, SD, USA. Appl. Environ Microbiol.

Chan C. S., De Stasio G., Welch S. A., Girasole M., Frazer B. H., Nesterova M. V., Fakra S. and Banfield J. F. (2004) Microbial Polysaccharides Template Assembly of Nanocrystal Fibers. *Science (80-.)*. **1656**, 10–13.

Chan, C.S., Fakra, S.C., Emerson, D., Fleming, E.J., Edwards, K.J., 2011. Lithotrophic iron-oxidizing bacteria produce organic stalks to control mineral growth: Implications for biosignature formation. ISME J. 5, 717–727.

Chang, L., Roberts, A.P., Tang, Y., Rainford, B.D., Muxworthy, A.R., Chen, Q., 2008. Fundamental magnetic parameters from pure synthetic greigite (Fe3S4). J. Geophys. Res. Solid Earth 113, 1–16.

Chaumeil, P.A., Mussig, A.J., Hugenholtz, P., Parks, D.H., 2022. GTDB-Tk v2: memory friendly classification with the genome taxonomy database. Bioinformatics 38, 5315–5316.

Chen, S., Zhou, Y., Chen, Y., Gu, J., 2018. Fastp: An ultra-fast all-in-one FASTQ preprocessor. Bioinformatics 34, i884–i890.

Chklovski, A., Parks, D.H., Woodcroft, B.J., Tyson, G.W., 2022. CheckM2: a Rapid, Scalable and Accurate Tool for Assessing Microbial Genome Quality Using Machine Learning. bioRxiv 1–24.

Claret, F., Bauer, A., Schäfer, T., Griffault, L., Lanson, B., 2002. Experimental investigation of the interaction of clays with high-pH solutions: A case study from the Callovo-Oxfordian formation, Meuse-Haute Marne underground laboratory (France). Clays Clay Miner. 50, 633–646.

Cloud Jr., P.E., Gruner, J.W., Hagen, H., 1965. Carbonaceous Rocks of the Soudan Iron Formation (Early Precambrian). Science 80-.). 148, 1713–1716.

Csákberényi-Malasics, D., Rodriguez-Blanco, J.D., Kis, V.K., Rečnik, A., Benning, L.G., Pósfai, M., 2012. Structural properties and transformations of precipitated FeS. Chem. Geol. 294–295, 249–258.

De Cáceres, M., Legendre, P., 2009. Associations between species and groups of sites: indices and statistical inference. Ecology 90, 3566–3574.

Dowd, W.S., Schuler, C.J., Santelli, C.M., Toner, B.M., Sheik, C.S., Pehr, K., Mcdermott, J. M., 2022. Potential energy sources for the deep continental biosphere in isolated anoxic brines. Earth Planet. Sci. Lett. 595, 117720.

Dutta, A., Sar, P., Sarkar, J., Dutta, G.S., Gupta, A., Bose, H., Mukherjee, A., Roy, S., 2019. Archaeal Communities in Deep Terrestrial Subsurface Underneath the Deccan Traps, India. *Front. Microbiol.* 10, 1–18.

Edwards, R.A., Rodriguez-Brito, B., Wegley, L., Haynes, M., Breitbart, M., Peterson, D.M., Saar, M.O., Alexander, S., Alexander, E.C., Rohwer, F., 2006. Using pyrosequencing to shed light on deep mine microbial ecology. BMC Genomics 7, 1–13.

Elsgaard, L., Jørgensen, B.B., 1992. Anoxic transformations of radiolabeled hydrogen sulfide in marine and freshwater sediments. Geochim. Cosmochim. Acta 56, 2425–2435.

Escudero, C., Vera, M., Oggerin, M., Amils, R., 2018. Active microbial biofilms in deep poor porous continental subsurface rocks. Sci. Rep. 8, 1–9.

Ferguson, G., McIntosh, J., Warr, O., Sherwood, L.B., 2023. The low permeability of the Earth's Precambrian crust. Commun. Earth Environ. 4, 1–8.

Flemming, H.C., Wuertz, S., 2019. Bacteria and archaea on Earth and their abundance in biofilms. Nat. Rev. Microbiol. 17, 247–260.

Frape, S.K., Fritz, P., McNutt, R.H., 1984. Water-rock interaction and chemistry of groundwaters from the Canadian Shield. Geochim. Cosmochim. Acta 48, 1617–1627.
Fritz, P., Frape, S.K., 1982. Saline groundwaters in the Canadian Shield - A first overview. Chem. Geol. 36, 179–190.
Fritz, P., Frape, S.K., Drimmie, R.J., Appleyard, E.C., Hattori, K., 1994. Sulfate in brines in the crystalline rocks of the Canadian shield. Geochim. Cosmochim. Acta 58, 57–65.
Garber, A.I., Nealson, K.H., Okamoto, A., McAllister, S.M., Chan, C.S., Barco, R.A., Merino, N., 2020. FeGenie: A Comprehensive Tool for the Identification of Iron Genes and Iron Gene Neighborhoods in Genome and Metagenome Assemblies. Front. Microbiol. 11, 1–23.
Gascoyne, M., 2004. Hydrogeochemistry, groundwater ages and sources of salts in a granitic batholith on the Canadian Shield, southeastern Manitoba. Appl. Geochemistry 19, 519–560.
Haveman, S.A., Pedersen, K., Ruotsalainen, P., 1999. Distribution and metabolic diversity of microorganisms in deep igneous rock aquifers of Finland. Geomicrobiol. J. 16, 277–294.
Hazen, T.C., Jiménez, L., López de Victoria, G., Fliermans, C.B., 1991. Comparison of bacteria from deep subsurface sediment and adjacent groundwater. Microb. Ecol. 22, 293–304.
Heinemann, N., Alcalde, J., Miocic, J.M., Hangx, S.J.T., Kallmeyer, J., Ostertag-Henning, C., Hassanpouryouzband, A., Thaysen, E.M., Strobel, G.J., Schmidt-Hattenberger, C., Edlmann, K., Wilkinson, M., Bentham, M., Stuart, H.R., Carbonell, R., Rudloff, A., 2021. Enabling large-scale hydrogen storage in porous media-the scientific challenges. Energy Environ. Sci. 14, 853–864.
Herbert, R.B., Benner, S.G., Pratt, A.R., Blowes, D.W., 1998. Surface chemistry and morphology of poorly crystalline iron sulfides precipitated in media containing sulfate-reducing bacteria. Chem. Geol. 144, 87–97.
Hitchcock A. (2021) aXis2000 - Analyis of X-ray Images and Spectra.
Hoffman, C.L., Nicholas, S.L., Ohnemus, D.C., Fitzsimmons, J.N., Sherrell, R.M., German, C.R., Heller, M.I., Lee, J., Lam, P.J., Toner, B.M., 2018. Near-field iron and carbon chemistry of non-buoyant hydrothermal plume particles, Southern East Pacific Rise 15°S. Mar. Chem. 201, 183–197.
Holloway, S., 1997. An Overview of the Underground Disposal of Carbon Dioxide. Energy Convers. Manag. 38, 193–198.
Holmkvist, L., Ferdelman, T.G., Jørgensen, B.B., 2011. A cryptic sulfur cycle driven by iron in the methane zone of marine sediment (Aarhus Bay, Denmark). Geochim. Cosmochim. Acta 75, 3581–3599.
Horiuchi, S., Wada, H., Moori, T., 1974. Morphology and imperfection of hydrothermally synthesized greigite (Fe3S4). J. Cryst. Growth 24–25, 624–626.
Hubalek, V., Wu, X., Eiler, A., Buck, M., Heim, C., Dopson, M., Bertilsson, S., Ionescu, D., 2016. Connectivity to the surface determines diversity patterns in subsurface aquifers of the Fennoscandian shield. ISME J. 10, 2447–2458.
Hunger, S., Benning, L.G., 2007. Greigite: A true intermediate on the polysulfide pathway to pyrite. Geochem. Trans. 8, 1–20.
Itävaara, M., Nyyssönen, M., Kapanen, A., Nousiainen, A., Ahonen, L., Kukkonen, I., 2011. Characterization of bacterial diversity to a depth of 1500m in the Outokumpu deep borehole, Fennoscandian Shield. *FEMS Microbiol. Ecol.* 77, 295–309.
Jagevall, S., Rabe, L., Pedersen, K., 2011. Abundance and Diversity of Biofilms in Natural and Artificial Aquifers of the Äspö Hard Rock. Microb. Ecol. 61, 410–422.
Jeong, H.Y., Han, Y.S., Park, S.W., Hayes, K.F., 2010. Aerobic oxidation of mackinawite (FeS) and its environmental implication for arsenic mobilization. Geochim. Cosmochim. Acta 74, 3182–3198.
Jiménez, O.F., Chan, C.H., Bond, D.R., 2018. Identification of Different Putative Outer Membrane Electron Conduits Necessary for Fe(III) Citrate, Fe(III) Oxide, Mn(IV) Oxide, or Electrode Reduction by Geobacter sulfurreducens. J. Bacteriol. 200, 1–20.
Jones, A.A., Bennett, P.C., 2017. Mineral ecology: Surface specific colonization and geochemical drivers of biofilm accumulation, composition, and phylogeny. Front. Microbiol. 8, 1–14.
Jørgensen, B.B., Findlay, A.J., Pellerin, A., 2019. The biogeochemical sulfur cycle of marine sediments. Front. Microbiol. 10, 1–27.
Kang, D.D., Li, F., Kirton, E., Thomas, A., Egan, R., An, H., Wang, Z., 2019. MetaBAT 2: An adaptive binning algorithm for robust and efficient genome reconstruction from metagenome assemblies. PeerJ 2019, 1–13.
Kelly D. P. and Wood A. P. (2000) Reclassification of some species of Thiobacillus to the newly designated genera Acidithiobacillus gen. nov., Halothiobacillus gen. nov. and Thermithiobacillus gen. nov. *Int. J. Syst. Evol. Microbiol.*, 511–516.
Kieft, T.L., McCuddy, S.M., Onstott, T.C., Davidson, M., Lin, L.H., Mislowack, B., Pratt, L., Boice, E., Lollar, B.S., Lippmann-Pipke, J., Pfiffner, S.M., Phelps, T.J., Gihring, T., Moser, D., van Heerden, A., 2005. Geochemically generated, energy-rich substrates and indigenous microorganisms in deep, ancient groundwater. Geomicrobiol. J. 22, 325–335.
Kieft, T.L., Walters, C.C., Higgins, M.B., Mennito, A.S., Clewett, C.F.M., Heuer, V., Pullin, M.J., Hendrickson, S., van Heerden, E., Sherwood, L.B., Lau, M.C.Y., Onstott, T.C., 2018. Dissolved organic matter compositions in 0.6–3.4 km deep fracture waters, Kaapvaal Craton. South Africa. *Org. Geochem.* 118, 116–131.
Kilcoyne, A.L.D., Tyliszczak, T., Steele, W.F., Fakra, S., Hitchcock, P., Franck, K., Anderson, E., Harteneck, B., Rightor, E.G., Mitchell, G.E., Hitchcock, A.P., Yang, L., Warwick, T., Ade, H., 2003. Interferometer-controlled scanning transmission X-ray microscopes at the Advanced Light Source. J. Synchrotron Radiat. 10, 125–136.
Kjeldsen, K.U., Schreiber, L., Thorup, C.A., Boesen, T., Bjerg, J.T., Yang, T., Dueholm, M. S., Larsen, S., Risgaard-Petersen, N., Nierychlo, M., Schmid, M., Bøggild, A., de Vossenberg, J. van, Geelhoed, J.S., Meysman, F.J.R., Wagner, M., Nielsen, P.H., Nielsen, L.P., Schramm, A., 2019. On the evolution and physiology of cable bacteria. Proc. Natl. Acad. Sci. USA 116, 19116–19125.
Klinger, F., 1958. Exploration Drill Hole Record: DDH 932. Eveleth, MN.
Kloppmann, W., Girard, J.P., Négrel, P., 2002. Exotic stable isotope compositions of saline waters and brines from the crystalline basement. Chem. Geol. 184, 49–70.
Krumholz, L.R., Mckinley, J.P., Ulrich, G.A., Suflita, J.M., 1997. Confined subsurface microbial communities in Cretaceous rock. Nature 386, 64–66.
Labrenz, M., Collins, M.D., Lawson, P.A., Tindall, B.J., Schumann, P., Hirsch, P., 1999. Roseovarius tolerans gen. nov., sp. nov., a budding bacterium with variable bacteriochlorophyll a production from hypersaline Ekho Lake. Int. J. Syst. Bacteriol. 49, 137–147.
Lai, M.-C., 2019. Methanolobus. Bergey's Man. Syst, Archaea Bact.
Langwig, M.V., De, A.V., Teske, A.P., Baker, B.J., Dombrowski, N., Seitz, K.W., Rambo, I. M., Greening, C., 2022. Large-scale protein level comparison of Deltaproteobacteria reveals cohesive metabolic groups. ISME J.
Laska, S., Lottspeich, F., Kletzin, A., 2003. Membrane-bound hydrogenase and sulfur reductase of the hyperthermophilic and acidophilic archaeon Acidianus ambivalens. Microbiology 2357–2371.
Lau, M.C.Y., Kieft, T.L., Kuloyo, O., Linage-Alvarez, B., Van Heerden, E., Lindsay, M.R., Magnabosco, C., Wang, W., Wiggins, J.B., Guo, L., Perlman, D.H., Kyin, S., Shwe, H. H., Harris, R.L., Oh, Y., Yi, M.J., Purtschert, R., Slater, G.F., Ono, S., Wei, S., Li, L., Lollar, B.S., Onstott, T.C., 2016. An oligotrophic deep-subsurface community dependent on syntrophy is dominated by sulfur-driven autotrophic denitrifiers. Proc. Natl. Acad. Sci. u. s. a. 113, 927–936.
Lawrence, J.R., Swerhone, G.D.W., Leppard, G.G., Araki, T., Zhang, X., West, M.M., Hitchcock, A.P., 2003. Scanning transmission X-ray, laser scanning, and transmission electron microscopy mapping of the exopolymeric matrix of microbial biofilms. Appl. Environ. Microbiol. 69, 5543–5554.
Lee, S.H., Secchi, E., Kang, P.K., 2023. Rapid formation of bioaggregates and morphology transition to biofilm streamers induced by pore-throat flows. Proc. Natl. Acad. Sci. 120, 1–10.
Lehman, R.M., Colwell, F.S., Bala, G.A., 2001. Attached and Unattached Microbial Communities in a Simulated Basalt Aquifer under Fracture- and Porous-Flow Conditions. Appl. Environ. Microbiol. 67, 2799–2809.
Lehmann J., Solomon D., Brandes J., Fleckenstein H., Jacobson C. and Thieme J. (2009) Synchrotron-Based Near-Edge X-Ray Spectroscopy of Natural Organic Matter in Soils and Sediments. In *Biophysico-Chemical Processes Involving Natural Nonliving Organic Matter in Environmental Systems* (eds. N. Senesi, B. Xing, and P. M. Huang). John Wiley & Sons. pp. 729–781.
Li, L., Wing, B.A., Bui, T.H., McDermott, J.M., Slater, G.F., Wei, S., Lacrampe-Couloume, G., Lollar, B.S., 2016. Sulfur mass-independent fractionation in subsurface fracture waters indicates a long-standing sulfur cycle in Precambrian rocks. Nat. Commun. 7, 1–9.
Lin, L., Wang, P., Rumble, D., Lippmann-pipke, J., Pratt, L.M., Sherwood-Lollar, B., Brodie, E.L., Hazen, T.C., Andersen, G.L., Desantis, T.Z., Moser, D.P., Kershaw, D., Onstott, T.C., 2006. Long-Term Sustainability of a High-Energy, Low-Diversity Crustal Biome. Science (80-.). 314, 479–482.
Lovley, D.R., Chapelle, F.H., 1995. Deep Subsurface Microbial Processes. Rev. Geophys. 33, 365–381.
Lovley, D.R., Phillips, E.J.P., Lonergan, D.J., 1991. Enzymatic versus Nonenzymatic Mechanisms for Fe(III) Reduction in Aquatic Sediments. Environ. Sci. Technol. 25, 1062–1067.
Luther, G.W., Kostka, J.E., Church, T.M., Sulzberger, B., Stumm, W., 1992. Seasonal iron cycling in the salt-marsh sedimentary environment: the importance of ligand complexes with Fe(II) and Fe(III) in the dissolution of Fe(III) minerals and pyrite, respectively. Mar. Chem. 40, 81–103.
MacLean, L.C.W., Pray, T.J., Onstott, T.C., Brodie, E.L., Hazen, T.C., Southam, G., 2007. Mineralogical, chemical and biological characterization of an anaerobic biofilm collected from a borehole in a deep gold mine in South Africa. Geomicrobiol. J. 24, 491–504.
Magnabosco, C., Lin, L.H., Dong, H., Bomberg, M., Ghiorse, W., Stan-Lotter, H., Pedersen, K., Kieft, T.L., van Heerden, E., Onstott, T.C., 2018a. The biomass and biodiversity of the continental subsurface. Nat. Geosci. 11, 707–717.
Magnabosco, C., Timmers, P.H.A., Lau, M.C.Y., Borgonie, G., Linage-Alvarez, B., Kuloyo, O., Alleva, R., Kieft, T.L., Slater, G.F., van Heerden, E., Sherwood, L.B., Onstott, T.C., 2018b. Fluctuations in populations of subsurface methane oxidizers in coordination with changes in electron acceptor availability. FEMS Microbiol. Ecol. 94, 1–10.
Marcus M. A. (2022) STXM Image Reader.
McMahon, S., Parnell, J., 2014. Weighing the deep continental biosphere. FEMS Microbiol. Ecol. 87, 113–120.
Meyer, B., Kuever, J., 2007. Molecular analysis of the distribution and phylogeny of dissimilatory adenosine-5'-phosphosulfate reductase-encoding genes (aprBA) among sulfur-oxidizing. Microbiology 153, 3478–3498.
Michel, F.M., Ehm, L., Antao, S.M., Lee, P.L., Chupas, P.J., Liu, G., Strongin, D.R., Schoonen, M.A.A., Phillips, B.L., Parise, J.B., 2007. The structure of ferrihydrite, a nanocrystalline material. Science (80-.) 316, 1726–1729.
Momper, L., Jungbluth, S.P., Lee, M.D., Amend, J.P., 2017a. Energy and carbon metabolisms in a deep terrestrial subsurface fluid microbial community. ISME J. 11, 2319–2333.
Momper, L., Kiel, R.B., Zinke, L., Wanger, G., Osburn, M.R., Moser, D., Amend, J.P., 2017b. Major phylum-level differences between porefluid and host rock bacterial communities in the terrestrial deep subsurface. Environ. Microbiol. Rep. 9, 501–511.
Morse, J.W., Millero, F.J., Cornwell, J.C., Rickard, D., 1987. The Chemistry of the Hydrogen Sulfide and Iron Sulfide Systems in Natural Waters. Earth-Science Rev. 24, 1–42.
Moser, D.P., Gihring, T.M., Fredrickson, J.K., Balkwill, D.L., Dollhopf, M.E., Pratt, L.M., Boice, E., Southam, G., Wanger, G., Baker, B.J., Pfiffner, S.M., Lin, L., Onstott, T.C.,

2005. Desulfotomaculum and Methanobacterium spp. Dominate a 4- to 5-Kilometer-Deep Fault. Appl. Environ. Microbiol. 71, 8773–8783.
Muyzer, G., Stams, A.J.M., 2008. The ecology and biotechnology of sulphate-reducing bacteria. Nat. Rev. Microbiol. 6, 441–454.
Newville, M., 2013. Larch: An analysis package for XAFS and related spectroscopies. J. Phys. Conf. Ser. 430.
Ng, G.H.C., Rosenfeld, C.E., Santelli, C.M., Yourd, A.R., Lange, J., Duhn, K., Johnson, N. W., 2020. Microbial and Reactive Transport Modeling Evidence for Hyporheic Flux-Driven Cryptic Sulfur Cycling and Anaerobic Methane Oxidation in a Sulfate-Impacted Wetland-Stream System. J. Geophys. Res. Biogeosciences 125, 1–25.
Nico, P.S., Regier, T.Z., Gillespie, A.W., Cismasu, A.C., 2017. Carbon near-edge absorption fine structure as a tool for understanding chemical differences in biochars. In: *Biochar: A Guide to Analytical Methods CSIRO Publishing, Clayton South, VIC, Australia*, pp. 214–228.
Nuppunen-Puputti, M., Kietäväinen, R., Purkamo, L., Rajala, P., Itävaara, M., Kukkonen, I., Bomberg, M., 2021. Rock surface fungi in deep continental biosphere—exploration of microbial community formation with subsurface in situ biofilm trap. Microorganisms 9, 1–29.
Nuppunen-Puputti, M., Kietäväinen, R., Raulio, M., Soro, A., Purkamo, L., Kukkonen, I., Bomberg, M., 2022. Epilithic Microbial Community Functionality in Deep Oligotrophic Continental Bedrock. Front. Microbiol. 13, 1–23.
Nurk, S., Meleshko, D., Korobeynikov, A., Pevzner, P.A., 2017. MetaSPAdes: A new versatile metagenomic assembler. Genome Res. 27, 824–834.
Olson, G.J., Dockins, W.S., McFeters, G.A., Iverson, W.P., 1981. Sulfate-reducing and methanogenic bacteria from deep aquifers in montana. Geomicrobiol. J. 2, 327–340.
Onstott, T.C., Lin, L.H., Davidson, M., Mislowack, B., Borcsik, M., Hall, J., Slater, G., Ward, J., Sherwoodlollar, B., Lippmann-Pipke, J., Boice, E., Pratt, L.M., Pfiffner, S., Moser, D., Gihring, T., Kieft, T.L., Phelps, T.J., Vanheerden, E., Litthaur, D., Deflaun, M., Rothmel, R., Wanger, G., Southam, G., 2006. The origin and age of biogeochemical trends in deep fracture water of the witwatersrand basin, south africa. Geomicrobiol. J. 23, 369–414.
Onstott, T.C., McGown, D.J., Bakermans, C., Ruskeeniemi, T., Ahonen, L., Telling, J., Soffientino, B., Pfiffner, S.M., Sherwood-Lollar, B., Frape, S., Stotler, R., Johnson, E. J., Vishnivetskaya, T.A., Rothmel, R., Pratt, L.M., 2009. Microbial communities in subpermafrost saline fracture water at the Lupin Au mine, Nunavut. Canada. *Microb. Ecol.* 58, 786–807.
Pedersen, K., 1997. Microbial life in deep granitic rock. FEMS Microbiol. Rev. 20, 399–414.
Pedersen, K., Arlinger, J., Ekendahl, S., Hallbeck, L., 1996. 16S rRNA gene diversity of attached and unattached bacteria in boreholes along the access tunnel to the Äspö hard rock laboratory, Sweden. *FEMS Microbiol. Ecol.* 19, 249–262.
Pellerin, A., Antler, G., Røy, H., Findlay, A., Beulig, F., Scholze, C., Turchyn, A.V., Jørgensen, B.B., 2018. The sulfur cycle below the sulfate-methane transition of marine sediments. Geochim. Cosmochim. Acta 239, 74–89.
Peterson, D.M., Patelke, R.L., 2003. National Underground Science and Engineering Laboratory (NUSEL): Geological site investigation for the Soudan Mine. Northeastern Minnesota, Duluth, MN.
Picard, A., Gartman, A., Clarke, D.R., Girguis, P.R., 2018. Sulfate-reducing bacteria influence the nucleation and growth of mackinawite and greigite. Geochim. Cosmochim. Acta 220, 367–384.
Poulton, S.W., Krom, M.D., Raiswell, R., 2004. A revised scheme for the reactivity of iron (oxyhydr)oxide minerals towards dissolved sulfide. Geochim. Cosmochim. Acta 68, 3703–3715.
Prescher, C., Prakapenka, V.B., 2015. DIOPTAS: A program for reduction of two-dimensional X-ray diffraction data and data exploration. High Press. Res. 35, 223–230.
Price M. (2023) fast.genomics.
Putz H. and Brandenburg K. (2003) Match! - Phase Identification from Powder Diffraction.
Pyzik, A.J., Sommer, S.E., 1981. Sedimentary iron monosulfides: kinetics and mechanism of formation. Geochim. Cosmochim. Acta 45, 687–698.
Ramírez, G.A., Garber, A.I., Lecoeuvre, A., D'angelo, T., Wheat, C.G., Orcutt, B.N., 2019. Ecology of subseafloor crustal biofilms. Front. Microbiol. 10, 1–17.
Rickard, D.T., 1969. The Microbial Formation of Iron Sulphides. Stock. Contrib. Geol. 20, 104–116.
Rickard D. and Luther G. W. (2007) *Chemistry of iron sulfides*.
Santelli, C.M., Banerjee, N., Bach, W., Edwards, K.J., 2010. Tapping the Subsurface Ocean Crust Biosphere: Low Biomass and Drilling-Related Contamination Calls for Improved Quality Controls. Geomicrobiol. J. 27, 158–169.
Schoonen, M.A.A., Barnes, H.L., 1991a. Reactions forming pyrite and marcasite from solution: I. Nucleation of FeS2 below 100°C. Geochim. Cosmochim. Acta 55, 1495–1504.
Schoonen, M.A.A., Barnes, H.L., 1991b. Reactions forming pyrite and marcasite from solution: II. Via FeS precursors below 100 C. Geochim. Cosmochim. Acta 55, 1505–1514.
Schuler, C.J., Briscoe, L.J., Alexander, S.C., Alexander, E.C., Gralnick, J.A., Santelli, C.M., Toner, B.M., 2022. Water and Rock Chemistry Inform Our Understanding of the Deep Biosphere: Case Study in an Archaean Banded Iron Formation. Front. Earth Sci. 10, 1–17.
Sheik, C.S., Badalamenti, J.P., Telling, J., Hsu, D., Alexander, S.C., Bond, D.R., Gralnick, J.A., Lollar, B.S., Toner, B.M., 2021. Novel Microbial Groups Drive Productivity in an Archean Iron Formation. Front. Microbiol. 12.
Sieber, C.M.K., Probst, A.J., Sharrar, A., Thomas, B.C., Hess, M., Tringe, S.G., Banfield, J. F., 2018. Recovery of genomes from metagenomes via a dereplication, aggregation and scoring strategy. Nat. Microbiol. 3, 836–843.
Sivan, O., Antler, G., Turchyn, A.V., Marlow, J.J., Orphan, V.J., 2014. Iron oxides stimulate sulfate-driven anaerobic methane oxidation in seeps. Proc. Natl. Acad. Sci. u. s. a. 111, E4139–E4147.
Sorokin, D.Y., Tourova, T.P., Bezsoudnova, E.Y., Pol, A., Muyzer, G., 2007. Denitrification in a binary culture and thiocyanate metabolism in Thiohalophilus thiocyanoxidans gen. nov. sp. nov. - A moderately halophilic chemolithoautotrophic sulfur-oxidizing Gammaproteobacterium from hypersaline lakes. Arch. Microbiol. 187, 441–450.
Stevens, T.O., Mckinley, J.P., 1995. Lithoautotrophic Microbial Ecosystems in Deep Basalt Aquifers. Science (80-.) 270, 450–454.
Takii, S., Hanada, S., Tamaki, H., Ueno, Y., Sekiguchi, Y., Ibe, A., Matsuura, K., 2007. Dethiosulfatibacter aminovorans gen. nov., sp. nov., a novel thiosulfate-reducing bacterium isolated from coastal marine sediment via sulfate-reducing enrichment with Casamino acids. Int. J. Syst. Evol. Microbiol. 57, 2320–2326.
Thorup, C., Schramm, A., Findlay, A.J., Finster, K.W., Schreiber, L., 2017. Disguised as a sulfate reducer: Growth of the deltaproteobacterium Desulfurivibrio alkaliphilus by Sulfide Oxidation with Nitrate. Mbio 8, 1–9.
Toner, B.M., Fakra, S.C., Manganini, S.J., Santelli, C.M., Marcus, M.A., Moffett, J.W., Rouxel, O., German, C.R., Edwards, K.J., 2009. Preservation of iron(II) by carbon-rich matrices in a hydrothermal plume. Nat. Geosci. 2, 197–201.
Toner, B.M., German, C.R., Dick, G.J., Breier, J.A., 2016. Deciphering the Complex Chemistry of Deep-Ocean Particles Using Complementary Synchrotron X-ray Microscope and Microprobe Instruments. Acc. Chem. Res. 49, 128–137.
Treude, T., Krause, S., Maltby, J., Dale, A.W., Coffin, R., Hamdan, L.J., 2014. Sulfate reduction and methane oxidation activity below the sulfate-methane transition zone in Alaskan Beaufort Sea continental margin sediments : Implications for deep sulfur cycling. Geochim. Cosmochim. Acta 144, 217–237.
Uritskiy, G.V., DiRuggiero, J., Taylor, J., 2018. MetaWRAP—a flexible pipeline for genome-resolved metagenomic data analysis. Microbiome 6, 1–13.
Warr, O., Giunta, T., Onstott, T.C., Kieft, T.L., Harris, R.L., Nisson, D.M., Lollar, B.S., 2021. The role of low-temperature 18O exchange in the isotopic evolution of deep subsurface fluids. Chem. Geol. 561, 1–26.
Williams, K.H., Ntarlagiannis, D., Slater, L.D., Dohnalkova, A., Hubbard, S.S., Banfield, J. F., 2005. Geophysical imaging of stimulated microbial biomineralization. Environ. Sci. Technol. 39, 7592–7600.
Woodcroft B. (2021) CoverM.
Wu, X., Holmfeldt, K., Hubalek, V., Lundin, D., Åström, M., Bertilsson, S., Dopson, M., 2016. Microbial metagenomes from three aquifers in the Fennoscandian shield terrestrial deep biosphere reveal metabolic partitioning among populations. ISME J. 10, 1192–1203.
Wu, X., Pedersen, K., Edlund, J., Eriksson, L., Åström, M., Andersson, A.F., Bertilsson, S., Dopson, M., 2017. Potential for hydrogen-oxidizing chemolithoautotrophic and diazotrophic populations to initiate biofilm formation in oligotrophic, deep terrestrial subsurface waters. Microbiome 5, 1–13.
Zhang, L., Verstraete, W., de Lourdes Mendoza, M., Lu, Z., Liu, Y., Huang, G., Cai, L., 2016. Decrease of dissolved sulfide in sewage by powdered natural magnetite and hematite. Sci. Total Environ. 573, 1070–1078.
Zhou, Z., Tran, P.Q., Breister, A.M., Liu, Y., Kieft, K., Cowley, E.S., Karaoz, U., Anantharaman, K., 2022. METABOLIC: high-throughput profiling of microbial genomes for functional traits, metabolism, biogeochemistry, and community-scale functional networks. Microbiome 10, 1–22.
Zhu, X., Hitchcock, A.P., Le Nagard, L., Bazylinski, D.A., Morillo, V., Abreu, F., Leão, P., Lins, U., 2018. X-ray Absorption Spectroscopy and Magnetism of Synthetic Greigite and Greigite Magnetosomes in Magnetotactic Bacteria. Geomicrobiol. J. 35, 215–226.
Zopfi, J., Ferdelman, T.G., Fossing, H., 2007. Distribution and fate of sulfur intermediates—sulfite, tetrathionate, thiosulfate, and elemental sulfur—in marine sediments. Geol. Soc. Am. Spec. Pap. 379, 97–116.